

An updated list of AGILE bright γ -ray sources and their variability in pointing mode

F. Verrecchia^{1,2}, C. Pittori^{1,2}, A.W. Chen³, A. Bulgarelli⁴, M. Tavani^{5,6,7,8}, F. Lucarelli^{1,2}, P. Giommi^{1,9}, S. Vercellone¹¹, A. Pellizzoni¹⁰, A. Giuliani³, F. Longo^{12,13}, G. Barbiellini^{12,13,8}, M. Trifoglio⁴, F. Gianotti⁴, A. Argan⁵, L.A. Antonelli^{2,1}, P. Caraveo³, M. Cardillo^{5,6}, P. W. Cattaneo¹⁴, V. Cocco⁶, S. Colafrancesco^{2,23}, T. Contessi³, E. Costa⁵, E. Del Monte⁵, G. De Paris⁵, G. Di Cocco⁴, G. Di Persio⁵, I. Donnarumma⁵, Y. Evangelista⁵, G. Fanari¹, M. Feroci⁵, A. Ferrari^{8,15}, M. Fiorini³, F. Fornari³, F. Fuschino⁴, T. Froyland^{8,6}, M. Frutti⁵, M. Galli¹⁶, C. Labanti⁴, I. Lapshov⁵, F. Lazzarotto⁵, F. Liello⁵, P. Lipari^{17,18}, E. Mattaini², M. Marisaldi⁴, M. Mastropietro^{5,20}, A. Mauri⁴, F. Mauri¹⁴, S. Mereghetti², E. Morelli⁴, E. Moretti^{7,8}, A. Morselli⁷, L. Pacciani⁵, F. Perotti³, G. Piano^{5,8}, P. Picozza^{6,7}, M. Pilia^{22,10}, C. Pontoni^{8,5}, G. Porrovecchio⁵, M. Prest²¹, R. Primavera¹, G. Pucella¹⁹, M. Rapisarda¹⁹, A. Rappoldi¹⁴, E. Rossi⁴, A. Rubini⁵, S. Sabatini¹⁰, P. Santolamazza^{1,2}, P. Soffitta⁵, S. Stellato¹, E. Striani¹⁰, F. Tamburelli¹, A. Traci⁴, A. Trois¹⁰, E. Vallazza^{12,13}, V. Vittorini^{5,6}, D. Zanello^{17,18}, L. Salotti⁹ and G. Valentini⁹

Affiliations can be found after the references

Received 12 March 2013; Accepted 14 Jun 2013

ABSTRACT

Aims. We present a variability study of a sample of bright γ -ray (30 MeV – 50 GeV) sources. This sample is an extension of the first AGILE catalogue of γ -ray sources (1AGL), obtained using the complete set of AGILE observations in pointing mode performed during a 2.3 year period from July 9, 2007 until October 30, 2009.

Methods. The dataset of AGILE pointed observations covers a long time interval and its γ -ray data archive is useful for monitoring studies of medium-to-high brightness γ -ray sources. In the analysis reported here, we used data obtained with an improved event filter that covers a wider field of view, on a much larger (about 27.5 months) dataset, integrating data on observation block time scales, which mostly range from a few days to thirty days.

Results. The data processing resulted in a better characterized source list than 1AGL was, and includes 54 sources, 7 of which are new high galactic latitude ($|B||l| \geq 5$) sources, 8 are new sources on the galactic plane, and 20 sources from the previous catalogue with revised positions. Eight 1AGL sources (2 high-latitude and 6 on the galactic plane) were not detected in the final processing either because of low OB exposure and/or due to their position in complex galactic regions. We report the results in a catalogue of all the detections obtained in each single OB, including the variability results for each of these sources. In particular, we found that 12 sources out of 42 or 11 out of 53 are variable, depending on the variability index used, where 42 and 53 are the number of sources for which these indices could be calculated. Seven of the 11 variable sources are blazars, the others are Crab pulsar+nebula, LS I +61°303, Cyg X-3, and 1AGLR J2021+4030.

Key words. catalogs — γ -rays: general — γ -rays: galaxies

1. Introduction

The Astrorivelatore Gamma ad Immagini LEggero (AGILE) (Tavani et al. 2008; Tavani et al. 2009a) is a mission of the Italian Space Agency (ASI) dedicated to γ -ray and hard X-ray astrophysics in the 30 MeV – 50 GeV and 18 – 60 keV energy ranges, launched on April 23 2007.

AGILE is the first γ -ray mission to operate in space after the end of the EGRET (Thompson et al. 1993) observations, and has been the only mission entirely dedicated to high-energy astrophysics above 30 MeV until 2008. On 11 June 2008, the Fermi Gamma-Ray Space Telescope (Michelson 2008; Atwood et al. 2009) was launched, which is operating concurrently with AGILE. The AGILE spacecraft had operated in fixed-pointing mode since launch until October 2009, completing 101 pointings or observation blocks (OBs). Then, due to a failure of the spacecraft reaction wheel, the attitude control sys-

tem was reconfigured and the scientific mode of operation was changed to spinning mode. Currently, the instrument pointing direction scans the sky with an angular velocity of about $0.8^\circ/\text{s}$, resulting in an exposure of about $7 \times 10^6 \text{ cm}^2\text{s}$ for about 70% of the sky in one day. The best γ -ray sensitivity of AGILE is in the 100 MeV – 1 GeV energy band.

The first AGILE catalogue of high-confidence γ -ray sources (1AGLs; Pittori et al. 2009) included a significance-limited (4σ) sample of 47 sources, obtained with a conservative data analysis of the first-year inhomogeneous AGILE dataset. The second Fermi catalogue (2FGLs; Nolan et al. 2012) increased the number of known γ -ray sources to about 2000, with the established main classes of active galactic nuclei (AGN), pulsars (PSRs) and pulsar wind nebulae. Since the third EGRET source catalogue (3EG; Hartman et al. 1999), γ -ray source flux variability on a 15-day time scale has been an important criterion for selecting candidates for multi-wavelength campaigns (for example, Romero et al. 1999; Torres et al. 2001; Paredes et al. 2005).

Send offprint requests to: F. Verrecchia,
e-mail: francesco.verrecchia@asdc.asi.it

2FGL reported variability indices for each source over a monthly time scale.

We decided to study the flux variations of a sample of about 60 of the brightest sources over the OB time scale in the pointing mode phase, when the AGILE-GRID sensitivity was higher (the exposure efficiency per single source was 0.6 while that of Fermi/LAT is about 0.16, see Morselli et al. 2013).

In this paper we present the results of the variability study of a sample of 54 sources selected as a revision of the 1AGL, separately analysing each OB included in the 2.3 year dataset of AGILE pointed observations (see also Verrecchia et al. 2011). The source sample was obtained with a preliminary revision of the 1AGL sources on the maps obtained from the merging of data from the whole dataset (*deep* maps hereafter). We used a much larger dataset than for 1AGL and data from the latest event filter (*FM3.119*, also known as *FM*; Bulgarelli et al., 2009, 2010 and Bulgarelli et al., in prep.; Chen et al. 2011b, 2012 and Chen et al., 2013), which covers a wider field of view (FoV), which allowed us to obtain a more uniform sensitivity over most of the sky despite the pointing strategy chosen in that phase; the mean effective exposure is ~ 1800 Ms (see Fig. 1).

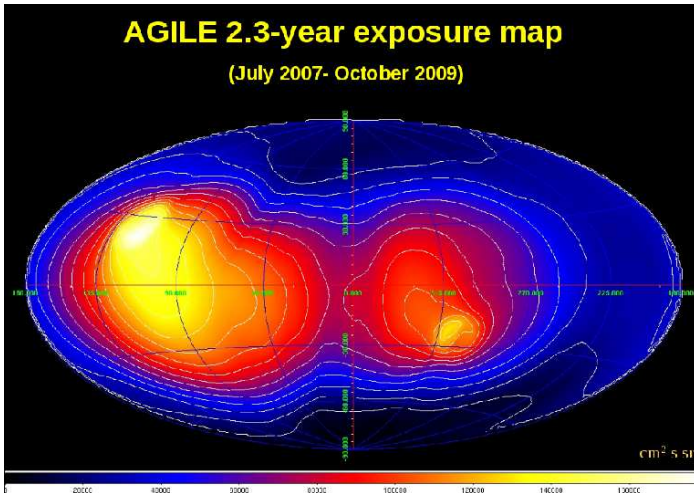


Fig. 1. AGILE-GRID 2.3 year all-sky exposure map in an Aitoff projection obtained with the *FM* event filter from all pointed-observations data (96 OBs).

We describe the AGILE-GRID performances and the OB data archive in Sections 2 and 3, the data analysis procedure in Section 4, and the variability analysis in Section 5. In Section 6 we present the results obtained, both the variability results and the catalogue of all *detections* in all OBs. We then discuss the results and report some final considerations in Section 7.

2. AGILE-GRID characteristics and calibration

The AGILE scientific payload consists of a silicon tracker imaging detector (Barbiellini et al. 2001, 2002; Prest et al. 2003), a CsI(Tl) mini-calorimeter detector (Labanti et al. 2006, 2009), and an anti-coincidence system (Perotti et al. 2006), which together form the Gamma-Ray Imaging Detector (GRID). It also features the X-ray coded mask silicon imaging detector SuperAGILE (Feroci et al. 2007). GRID is sensitive to photon energies in the 30 MeV – 50 GeV energy band, with a wide FoV (2.5 sr in pointing mode) and accurate timing (2 μ s), positional, and attitude information (15' location accuracy for $> 10\sigma$ detection).

The GRID calibration has been updated since the launch (Pittori et al. 2009; Bulgarelli et al. 2010; Cattaneo et al. 2011; Cattaneo et al. 2012; Chen et al. 2012). The GRID instrument energy-dependent point spread function (PSF), derived from in-flight calibrations, has a full-width at half-maximum (FWHM) of approximately 3.5° at 100 MeV and 0.7° at 1 GeV. The effective area is about 500 cm^2 at 300 MeV, depending on the event filter. Both GRID PSF and effective area have a very good off-axis performance and are well calibrated up to 60° , showing very smooth variations with the angle relative to the instrument axis. The version of the response matrices used in this analysis (I0010) was developed through the analysis of in-flight data to introduce flux corrections to improve the spectral response, taking into account the energy dispersion. They were created by comparing the fluxes obtained with the AGILE likelihood analysis of the Vela pulsar in each energy bin, with those expected from the fluxes and spectra reported in the first Fermi catalogue (Chen et al. 2012, 2013).

The *FM* filter has a FoV of $\sim 60^\circ$ radius, which is different from the *F4* filter used for the 1AGL, which was optimized only up to off-axis angles of $\sim 40^\circ$ radius.

The data analysis used the AGILE diffuse emission model (Giuliani et al. 2004) for diffuse γ -ray background as for the 1AGL, which substantially improves upon the previous one used by EGRET. It was obtained by using state-of-the-art maps of neutral hydrogen (Kalberla et al. 2005) and CO (Dame et al. 2001).

3. OB data archive

The AGILE baseline pointing plan during the pointing mode phase was defined before the beginning of each year's announcement of opportunity cycle to reach the goals that maximize the scientific output of the mission. The AGILE Data Center (ADC), part of the ASI Science Data Center (ASDC) in Frascati, Italy¹, is responsible for data reduction and scientific processing to create the official standard OB level-2 (LV2) data archive and distribute it to guest observers (GOs) or, when data become public, to the scientific community.

Raw data are routinely archived, transformed in FITS format (Trifoglio et al. 2008), and then processed using the official scientific data reduction and analysis software tasks (Bulgarelli et al. 2009; Chen et al. 2011b), which are integrated into an automatic quick-look (QL) pipeline system. The QL procedures perform data analysis on 1-, 2-, 3-, and 7-day time scales, including an automatic source detection and alert system (Bulgarelli et al. 2008). The final AGILE-GRID archive is created at the ADC after executing the OB standard analysis pipeline system. Both pipelines execute the event filter (based on a Kalman filter technique) for track identification, event direction, and energy reconstruction (Pittori & Tavani 2002; Giuliani et al. 2006)². The official OB pointing mode archive was built after removing data corresponding to slews and occasional losses of fine-pointing attitude, and it includes LV2 products, the spacecraft (LOG) and event (EVT) files, and the level-3 (LV3) counts, exposure and diffuse model maps. The OB LV3 maps used in this analysis were created in the $E > 100$ MeV energy band, with a bin of $0.25^\circ \times 0.25^\circ$, selecting events within 60° of the mean OB pointing direction and excluding photons

¹ <http://agile.asdc.asi.it>

² More details on the ADC organization and tasks will be given in a future publication (Pittori et al. in preparation).

Table 1. AGILE pointings in the period 9 July 2007 - 30 October 2009, corresponding to the 96 observation blocks (OB). Acronyms used in table are: ToO = target of opportunity pointing, SA = SuperAGILE special pointing.

Target Name	OB Number	Starting RA, Dec J2000 (deg)	Starting LLI, BII (deg)	Start/End Time (UTC)	Duration (days)	Target Name	OB Number	Starting RA, Dec J2000 (deg)	Starting LLI, BII (deg)	Start/End Time (UTC)	Duration (days)
3C279 Region	900	195.60, -6.65	307.81, 56.12	2007-07-09 12:00:07-07-13 12:00	4	South Gal. Pole	5220	65.66, -35.71	237.50, -44.67	2008-02-12 12:00:08-02-14 12:00	2
VELA Region	1000	157.98, -60.21	286.42, -1.90	2007-07-13 12:00:07-07-24 12:00	11	Repointing	5300	191.93, -71.89	302.64, -9.02	2008-02-14 12:00:08-03-01 12:00	14
ToO 3C 454.3	1100	17.83, 36.70	127.36, -26.01	2007-07-24 12:00:07-07-30 12:00	6	Musca Field	5400	243.60, -50.98	332.11, 0.02	2008-03-01 12:00:08-03-16 12:00	15
VELA Region	1150	17.83, 36.70	127.36, -26.01	2007-07-24 12:00:07-07-30 12:00	6	Gal. Center 1	5450	265.78, -28.63	359.98, 0.63	2008-03-16 12:00:08-03-30 12:00	14
VELA Region	1200	150.84, -70.19	289.53, -11.83	2007-07-30 12:00:07-08-01 12:00	2	Gal. Center 2	5500	100.94, 21.71	192.64, 8.11	2008-03-30 12:00:08-04-05 12:00	6
SA Crab -45	1300	37.10, 12.71	156.59, -43.73	2007-08-01 12:00:07-08-02 12:00	1	Anti-Center 1	5510	108.28, 28.63	188.96, 17.00	2008-04-05 12:00:08-04-07 12:00	2
VELA Region	1400	176.01, -66.06	296.16, -4.08	2007-08-02 12:00:07-08-12 12:00	10	SA Crab (8,24)	5520	111.76, 35.69	183.01, 22.20	2008-04-07 12:00:08-04-08 12:00	1
SA Crab -35	1500	47.41, 16.08	164.83, -35.32	2007-08-12 12:00:07-08-13 12:00	1	SA Crab (15,26)	5530	110.40, 20.76	197.30, 15.72	2008-04-08 12:00:08-04-10 12:00	2
VELA Region	1600	195.55, -66.56	304.00, -3.72	2007-08-13 12:00:07-08-23 12:00	9	Anti-Center 2	5550	110.40, 20.76	197.30, 15.72	2008-04-10 12:00:08-04-30 12:00	20
SA Crab -25	1700	57.14, 18.57	171.08, -27.31	2007-08-22 12:00:07-08-23 12:00	1	Vulpecula Field	5600	286.26, 20.82	53.04, 6.47	2008-04-30 12:00:08-05-10 12:00	10
VELA Region	1800	216.98, -64.44	313.11, -3.49	2007-08-23 12:00:07-08-27 12:00	4	North Gal. Pole	5700	250.08, 72.50	104.85, 35.44	2008-05-10 12:00:08-06-09 18:00	30.1
Galactic Plane	1900	236.57, -41.87	334.44, 10.06	2007-08-27 12:00:07-09-01 12:00	4	Cygnus Field 2	5800	304.29, 35.97	74.05, 0.27	2008-06-09 18:00:08-06-15 12:00	5.9
SA Crab (15,15)	2000	69.48, 5.59	190.90, -26.29	2007-09-01 12:00:07-09-02 12:00	1	ToO WComae/	5810	182.29, 29.61	195.50, 80.37	2008-06-15 12:00:08-06-30 12:00	15
SA Crab (0,15)	2100	68.21, 20.57	177.13, -18.28	2007-09-02 12:00:07-09-03 12:00	1	ON+231	5820	323.25, 50.08	93.66, -1.17	2008-06-30 12:00:08-07-25 18:00	25
SA Crab (-15,15)	2200	66.65, 35.56	164.63, -9.35	2007-09-03 12:00:07-09-04 12:00	1	Cygnus Repointing	5900	161.83, -47.73	282.31, 10.11	2008-07-25 18:00:08-07-31 12:00	5.9
Field 8	2300	51.41, 71.02	134.88, 11.82	2007-09-04 12:00:07-09-12 12:00	8	Antlia Field	5910	19.17, 38.09	128.56, -24.49	2008-07-31 12:00:08-08-15 12:00	15
SA Crab (0,5)	2400	78.54, 21.73	182.16, -9.89	2007-09-12 12:00:07-09-13 12:00	1	ToO 3C 454.3	5920	25.09, 40.12	330.46, 28.98	2008-08-15 12:00:08-08-31 12:00	16
Field 8	2500	74.88, 58.33	150.99, 9.73	2007-09-13 12:00:07-09-15 12:00	2	Estensio TOO	6010	175.31, -74.13	298.10, -11.92	2008-08-31 12:00:08-09-10 12:00	10
SA Crab (45,0)	2600	84.21, -23.01	226.70, -26.12	2007-09-15 12:00:07-09-16 12:00	1	3C454.3	6110	61.87, 44.06	333.90, 27.26	2008-09-10 12:00:08-10-10 12:00	30
SA Crab (5,0)	2700	82.99, 16.98	188.52, -8.98	2007-09-16 12:00:07-09-17 12:00	1	Musca Field 2	6200	256.55, -28.53	355.51, 7.40	2008-10-10 12:00:08-10-17 12:00	7
SA Crab (0,0)	2800	83.77, 22.03	184.62, -5.67	2007-09-17 12:00:07-09-18 12:00	1	ToO SGR 0501+4516	6310	98.80, -46.77	255.44, -22.05	2008-10-17 12:00:08-10-31 12:00	14
SA Crab (-5,0)	2900	84.62, 27.05	180.77, -2.33	2007-09-18 12:00:07-09-19 12:00	1	Gal. Center 3	6400	295.52, 35.64	70.03, 6.15	2008-10-31 12:00:08-11-30 12:00	30
SA Crab (-15,0)	3000	85.35, 37.09	172.59, 3.52	2007-09-19 12:00:07-09-20 12:00	1	ToO PKS 0537-441	6500	320.40, 35.50	81.95, -10.17	2008-11-30 12:00:08-12-20 12:00	23.1
SA Crab (-25,0)	3100	86.17, 47.12	164.26, 9.22	2007-09-20 12:00:07-09-21 12:00	1	Aquila Field	6600	334.10, 44.05	95.70, -10.47	2009-01-12 18:00:09-01-19 18:00	6.9
SA Crab (-35,0)	3200	87.14, 57.13	155.61, 14.60	2007-09-21 12:00:07-09-22 12:00	1	Cygnus Field 3	6610	161.67, -59.86	287.86, -0.69	2009-01-19 18:00:09-02-28 12:00	8.9
SA Crab (-45,0)	3300	88.35, 67.14	146.45, 19.48	2007-09-22 12:00:07-09-23 12:00	1	Cygnus Field 4	6710	325.75, 68.11	106.75, 11.37	2009-02-28 12:00:09-03-25 12:00	25
SA Crab (0,-5)	3400	90.10, 22.14	187.54, -0.59	2007-09-23 12:00:07-09-24 12:00	1	Cygnus Field 5	6800	247.20, -29.03	349.85, 13.43	2009-03-25 12:00:09-03-31 12:00	6
SA Crab (15,0)	3500	91.03, 7.14	201.11, -7.14	2007-09-24 12:00:07-09-25 12:00	1	ToO Carina Field	6810	275.73, -30.50	2.59, -7.83	2009-03-31 12:00:09-04-07 12:00	7
SA Crab (25,0)	3600	91.84, -2.88	210.46, -11.12	2007-09-25 12:00:07-09-26 12:00	1	Cygnus Field 6	6910	102.70, 31.71	184.07, 13.75	2009-04-07 12:00:09-04-15 12:00	8
SA Crab (35,0)	3700	92.50, -12.93	220.02, -14.95	2007-09-26 12:00:07-09-27 12:00	1	Gal.Center Prolonged	7010	288.88, -19.31	18.06, -13.82	2009-04-15 12:00:09-04-30 12:00	15
Crab Nebula	3800	94.32, 22.05	189.52, 2.80	2007-09-27 12:00:07-10-01 12:00	4	Crab Field	7100	290.88, 16.16	50.92, 0.44	2009-04-30 12:00:09-05-15 12:00	15
SA Crab (0,-15)	3900	98.55, 21.88	191.49, 6.19	2007-10-01 12:00:07-10-02 12:00	1	Aquila Field 1	7200	299.11, 29.78	66.49, -0.59	2009-05-15 12:00:09-05-29 12:00	10.1
SA Crab (-15,-15)	4000	100.84, 36.78	178.64, 14.35	2007-10-02 12:00:07-10-03 12:00	1	Vela Field 1	7300	127.35, -37.14	256.41, 1.08	2009-05-29 12:00:09-06-04 12:00	6
SA Crab (15,-15)	4100	99.57, 6.79	205.39, 0.18	2007-10-03 12:00:07-10-04 12:00	1	Vela Field 2	7310	328.44, 10.91	68.32, -32.54	2009-06-04 12:00:09-06-15 12:00	11
Crab Field	4200	101.72, 21.70	192.97, 8.76	2007-10-04 12:00:07-10-12 12:00	8	Cygnus Field 7	7320	136.50, -40.71	263.67, 4.38	2009-06-15 12:00:09-06-25 12:00	10
SA Crab (0,-25)	4300	110.13, 20.72	197.23, 15.47	2007-10-12 12:00:07-10-13 12:00	1	Cygnus Field 8	7410	167.14, 10.71	242.13, 60.76	2009-06-25 12:00:09-07-15 12:00	20
Gal. Center	4400	290.92, -18.90	19.27, -15.41	2007-10-13 12:00:07-10-22 12:00	9	Cygnus Field 9	7500	330.22, 43.11	92.83, -9.58	2009-07-15 12:00:09-08-12 12:00	28
SA Crab (0,-35)	4500	120.49, 18.88	203.04, 23.74	2007-10-22 12:00:07-10-23 12:00	1	Cygnus Field 10	7600	344.77, 37.90	99.66, -19.84	2009-08-12 12:00:09-08-31 12:00	19
Gal. Center Reg.	4600	301.17, -17.11	25.10, -23.67	2007-10-23 12:00:07-10-24 08:00	1	Vela Field 3	7700	202.30, -62.10	307.33, 0.45	2009-08-31 12:00:09-09-10 12:00	10
ToO 0716+714	4610	148.94, 67.89	143.36, 41.59	2007-10-24 08:00:07-10-29 12:00	5	Vela Field 4	7800	202.30, -62.10	307.33, 0.45	2009-09-10 12:00:09-09-13 12:00	3
ToO Extended	4630	157.46, 66.94	141.55, 44.72	2007-10-29 12:00:07-11-01 12:00	3	Cygnus Field 10	7900	243.77, -35.45	343.05, 11.11	2009-09-13 12:00:09-09-16 12:00	3
SA Crab (0,-45)	4700	130.61, 16.34	209.79, 31.74	2007-11-01 12:00:07-11-02 12:00	1	Vela Field 5	8000	78.33, -6.66	195.06, -18.31	2009-09-16 12:00:09-09-30 12:00	14
Cygnus Region	4800	296.88, 34.50	69.59, 4.62	2007-11-02 12:00:07-12-01 12:00	29	Normal Field	8100	81.78, -3.12	205.88, -20.15	2009-09-30 12:00:09-10-15 12:00	15
Cygnus Field 1	4900	304.43, 53.55	88.82, 9.93	2007-12-01 12:00:07-12-05 09:00	4	SA Crab (15,6)	8200	263.19, -23.49	232.78, -28.89	2009-10-15 12:00:09-10-31 12:00	16
Cygnus Repointing	4910	322.50, 38.24	85.12, -9.42	2007-12-05 09:00:07-12-15 12:00	10.1	SA Crab (25,3)	8300	278.13, -23.22	10.11, -6.45	2009-10-15 12:00:09-10-31 12:00	16
Cygnus Repointing	4920	322.50, 38.24	85.12, -9.42	2007-12-15 12:00:07-12-16 12:00	1	Galactic Center 5	8400	285.78, 28.82	60.12, 10.38	2009-10-15 12:00:09-10-31 12:00	16
Virgo Field	5010	173.43, -0.44	265.65, 56.70	2007-12-16 12:00:08-01-08 12:00	33	Aquila Field 3					
Vela Field	5100	147.06, -62.52	283.47, -6.79	2008-01-08 12:00:08-02-01 12:00	24	Aquila Field 4					
South Gal. Pole	5200	58.35, -37.80	240.39, -50.58	2008-02-01 12:00:08-02-09 09:00	8						
ToO MKN 421	5210	250.97, 50.29	77.31, 40.63	2008-02-09 09:00:08-02-12 12:00	3						

within 80° from the reconstructed satellite-Earth vector, to reduce γ -ray Earth-albedo contamination. This archive was created using the latest official version of the standard software and instrument response functions available at the time of the analysis³. The complete pointing mode OB archive⁴ is composed of 101 datasets with non-uniform exposures (from 1 to 45 days). We analysed the scientifically validated data archive that covers 2.3 years with 96 OBs (see Table 1), not including the first 5 OBs of the commissioning phase.

4. OB data analysis procedure

The procedure developed for the source analysis on the whole archive is based on point source detection at fixed preselected positions. The AGILE multi-source analysis task (ALIKE, Bulgarelli et al. 2009; Chen et al. 2011b), which we used to derive the best estimates of point source parameters, i.e. source significance, γ -ray flux, Galactic coordinates, and 95% confidence level (c.l.), is based on the maximum likelihood (ML) method. The ML method, used in previous γ -ray data analysis (Mattox et al. 1996) and for all recent AGILE and Fermi imaging results (see for instance Bulgarelli et al. 2012a; Bulgarelli et al. 2012b; Nolan et al. 2012), compares measured counts in each pixel with the predicted counts derived from a γ -ray model composed of the Galactic diffuse model (see Section 2), an isotropic diffuse component, and point sources modelled according to the instrument PSF. To reduce systematic errors that arise because the data were taken far away from the source, only data within a circle of a given radius around each source were used. The significance of a source detection is given by the test statistic TS, defined as the likelihood ratio, that is expected to behave as χ_1^2 in the null hypothesis for one single parameter that is to be optimized, i.e. the source flux. When m parameters must be optimized, the TS behaves as χ_m^2 .

We divide the procedure in three main steps:

- 1) the preliminary reanalysis of the 1AGL catalogue, mainly in complex Galactic plane regions, based on LV3 deep maps from the merging of all data in the OB archive, more recent AGILE results and including some high-latitude ($|BII| > 10^\circ$) sources detected in QL automatic procedures on a weekly time scale. The creation of the updated source list for next step;
- 2) the execution of a procedure based on the AGILE multi-source ML task on each OB LV3 map, first allowing source fluxes to vary while keeping source positions fixed, then allowing the source positions to vary;
- 3) the revision of the source list, taking into account the new results at fixed positions, for example when a source \sqrt{TS} is significantly changed (increased or decreased). The 95% c.l. contour obtained leaving the source position free was also checked to verify that contours of transient sources did not overlap the nearest source position.

where we used the \sqrt{TS} defined above as detection significance parameter.

The reanalysis of the 1AGL source positioning in step 1) is described in Section 4.1, followed by a description of step 2) in Section 4.2 and step 3) in Section 5.

³ Software build version: BUILD_GRID_STD_17 and BUILD_GRID_SCL19; calibration files version I0010.

⁴ Public OB archive is available at <http://www.asdc.asi.it/mmia/index.php?mission=agilemmia>.

4.1. Revision of the First AGILE-GRID catalogue based on the 2.3 yr dataset

The first AGILE catalogue (Pittori et al. 2009) was built using data collected during the first year of operations (July 2007 - June 2008), which includes half of cycle-1 of the AGILE GO program. The data analysis based on the conservative F4 filter, and the non-uniform sensitivity due to the inhomogeneous sky coverage during AGILE first year, limited the results in complex Galactic regions. We reanalyzed 1AGL sources in the Galactic plane regions, such as the Carina, LS I +61°303, Cygnus, Crux, and near the Galactic center, using the updated $E > 100$ MeV deep maps obtained from the merging of data up to October 2009 (Fig. 1) processed with the *FM* event filter. These maps were created using the event selections described in Section 3, using both $0.05^\circ \times 0.05^\circ$ and $0.1^\circ \times 0.1^\circ$ bins. We then built an updated reference list with improved source positions in these regions. We use the abbreviation "1AGLR" for the repositioned and new sources. First, we reanalyzed the low-significance ($3 \leq \sqrt{TS} \leq 4$) detections from the 1AGL processing in the Carina ($283^\circ < LII < 292^\circ$), LS I +61°303 ($130^\circ < LII < 136^\circ$) and Scutum-Sagittarius ($6^\circ < LII < 36^\circ$) regions, as well as four high-latitude detections at $\sqrt{TS} \geq 4$ not included in the catalogue (three of which are included in the final source list: 1AGLR J0135+4759, 1AGLR J0222+4305, 1AGLR J0321+4137). We then reanalyzed sources from more recently refined AGILE results in the Galactic plane (Tavani et al. 2009b, 2009c; Sabatini et al. 2010; Giuliani et al. 2010; Bulgarelli et al. 2012a; Piano et al. 2012).

We performed an ML multi-source analysis on the updated deep maps for these sources, to obtain the average fluxes used in the subsequent individual OB analyses. Two examples of source repositioning are shown in Fig. 2: a simple case for the high-latitude source 1AGLR J1848+6709 and a complex case for the Carina region. For this last case new source positions obtained in the ML analysis where source positions were allowed to vary, the 95% c.l. contour radii for the sources for which they were closed and their \sqrt{TS}_{deep} values are reported in Table 2. Two of these sources, 1AGLR J1022-5825 and 1AGLR J1107-6115, have been included in the list although they do not have a 95% c.l. contour from the ML analysis on deep maps. In these cases an additional \sqrt{TS}_{deep} value is shown, marked with an asterisk (\sqrt{TS}_{deep}^* hereafter); the value was obtained by keeping source position fixed.

We included 1AGLR J1022-5825 because it is only slightly repositioned with respect to 1AGL J1022-5822, whose error radius did not include the new sources (1AGLR J1018-5852, 1AGLR J1022-5751 and AGL J1029-5836), however, and also because it is significant on a single OB (7800) map. It was possible to obtain a detection at $\sqrt{TS} = 4.4$ on this OB, with an acceptable 95% c.l. contour, when allowing the source position to vary. Moreover, by executing an ML analysis on deep maps, keeping its position and the parameters of all nearby sources fixed, we obtained $\sqrt{TS}_{deep} = 4.0$. 1AGLR J1107-6115 was analogously included because of $\sqrt{TS}_{deep}^* \geq 4$ obtained with the deep maps at fixed position, and $\sqrt{TS} \geq 4$ in some OBs with an ML analysis with the parameters of all nearby sources (and of the diffuse emission) fixed. AGL J1029-5836 and AGL J1045-5736 (a repositioning of 1AGL J1043-5749), which have a \sqrt{TS}_{deep} above 5, were instead not significant over the OB time scale, and so do not appear in the final table.

Source Name	R.A., Dec. ($^{\circ}$)	95% Error Radius ($^{\circ}$)	\sqrt{TS}_{deep}
1AGLR J1018-5852	154.403, -58.860	0.25	10.5
1AGLR J1022-5751	155.389, -57.846	0.29	7.4
1AGLR J1022-5825	155.406, -58.423	–	<2, 4.0*
AGL J1029-5836	157.351, -58.608	0.36	5.0
AGL J1045-5736	161.253, -57.602	0.39	5.5
1AGLR J1044-5944	161.108, -59.734	0.25	4.9
1AGLR J1048-5843	161.887, -58.712	0.29	5.6
1AGLR J1107-6115	166.631, -61.257	–	<3, 4.1*
1AGLR J1112-6104	168.092, -61.073	0.44	5.4

Table 2. Revised γ -ray source list in the Carina region. 95% error radii are shown for the sources with closed contours. For 1AGLR J1022-5825 and 1AGLR J1107-6115, an additional \sqrt{TS}_{deep} value * is shown, obtained by keeping the source position fixed.

We also included seven sources detected in the QL processing on a weekly time scale with $\sqrt{TS} > 4$ at medium-high galactic latitude ($|BII| > 5^{\circ}$) to verify their significance on the non-uniform OB time scale. Only four of these were detected in our final processing and are included in the final source list described in Section 6 (they are 1AGLR J1625-2531, 1AGLR J1803-3941, 1AGLR J1833-2057, 1AGLR J2030-0617). The results from the QL processing on various time scales will be reported elsewhere.

We compared the results of each run with the input reference source list, revising it if needed. We took into account the 95% c.l. contours and the \sqrt{TS} , to check in detail candidate sources at fluxes $\sim 3.0 \times 10^{-7}$ ph cm $^{-2}$ s $^{-1}$ in the Carina, LS I +61 $^{\circ}$ 303, Scutum and 1AGLR J1625-2531 regions. This review resulted in the final version of the list, which includes 90 candidate sources. This source list was used as input in the following step.

A better characterization of complex Galactic regions will be reported in a future catalogue, implementing a new automatic source blind search.

4.2. Analysis of individual OBs

The ALIKE task is an iterative procedure that evaluates all the ML parameters that are left free to vary for each source in the input source list. We decided to fix the positions of all sources to reduce the number of parameters evaluated by the ALIKE task during the ML analysis in each single OB. This reduces the task running-time and can improve the precision of the results (see Bulgarelli et al. 2012b). For the same reason, we also fixed the spectral indices to -2.1 for all sources except for the five well-known bright pulsars Geminga, Crab, Vela, 1AGL J1709-4428, and 1AGLR J2021+3653 (fixed to -1.66 , -2.2 , -1.69 , -1.86 and -1.86 , from 3EG; Hartman et al. 1999; Chen et al. 2012), for 1AGLR J0007+7307, 1AGLR J2031+4130 and 1AGL J1836+5923 (fixed to -1.85 , -1.84 and -1.65 , from 3EG and Bulgarelli et al. 2008, 2012a), for the high-mass X-ray binaries (HMXBs) LS I +61 $^{\circ}$ 303 and Cyg X-3 (fixed to -2.21 and -2.0 from 3EG and Bulgarelli et al. 2012a) and the supernova remnants (SNRs) W28, IC443 and W44 (fixed to -1.8 , -2.01 and -1.93 from Giuliani et al. 2010, and 3EG respectively). These values are compatible with the 2FGL ones at the AGILE spectral resolution. In this analysis we used the ML task AG_multi2

included in the AGILE BUILD GRID_SCI_20 package and a circle of radius 10° for the ML analysis.

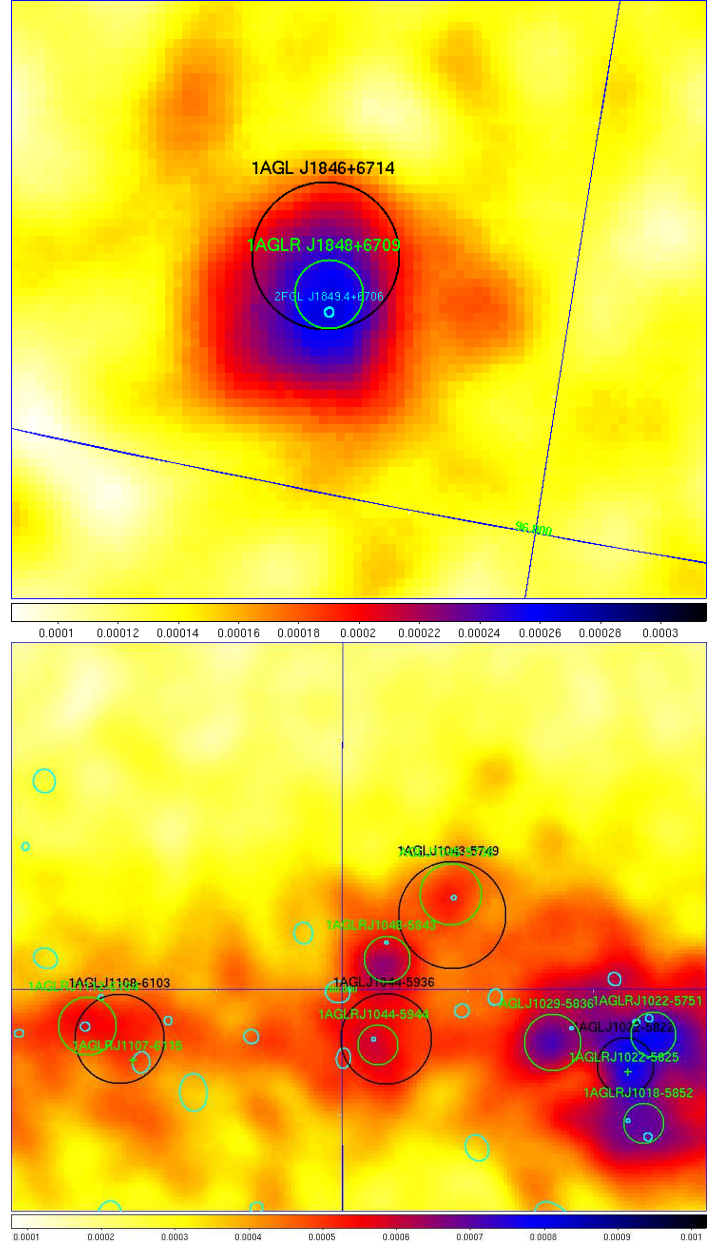


Fig. 2. Intensity maps of two 1AGL field refinements. In the first panel a simple case is shown, the high-latitude source 1AGL J1846+6714 repositioned to 1AGL J1848+6709. The new smaller error circle is indicated in green inside the 1AGL circle, while the 2FGL error ellipse is plotted in cyan. In the second panel a complex case is shown, the Carina region. New sources and new positions for 1AGL sources are indicated with a green circle, except for two sources for which no 95% c.l. contour has been obtained; their positions are indicated with crosses. The 1AGL error circles are indicated in black, the 2FGL error ellipses in cyan.

To improve the reference list (in conjunction with the creation of a reprocessed OB archive with a new software version), in particular the multi-source detection in complex regions, all steps of the analysis were repeated five times. Finally, we selected the results obtained with the last processing with source positions kept fixed to the last version of the reference source list

(see Section 5). Our goal was to refine multi-source detection in complex regions and add some high-latitude source, therefore we did not execute any automatic source detection process.

5. Detection selection and variability analysis

To investigate the variability within the OB dataset for established sources on deep maps and search for flaring episodes of sources with mean low significance, we analyzed the results from the last execution (the fifth) of the ML multi-source procedure on sources in the input reference list according to their significance and whether or not a 95% location contour could be found. We chose sources with either

- 1) both a high-significance detection ($\sqrt{TS} \geq 4$) from the deep map analysis and at least one OB detection with $\sqrt{TS} \geq 3$, or
- 2) at least one detection with $\sqrt{TS} \geq 4$ in a single OB. Moreover, we selected only sources with a 95% location contour from the deep map analysis (with a few exceptions, see section 4.1).

Then we checked each single OB detection with $3 \leq \sqrt{TS} < 4.5$, inspecting the single OB intensity map and checking the size and shape of the source 95% c.l. contours from the ML at free position, if present, to verify whether it overlapped the nearest sources. We thus excluded eight sources from the final source list. All sources in the last version of the reference list that do not appear in the catalogue table were not significant in our analysis according to these criteria.

We used the method developed by McLaughlin et al. (1996) that was recently used in the analysis of 1AGL J2022+4032 data (Chen et al. 2011a) to study the OB-scale γ -ray flux variability of the selected sources and report the results in the next section. We computed three versions of the variability index. To calculate the traditional index V , we computed the weighted mean flux, its error, and the χ^2 from the fluxes and errors in each OB. We evaluated the probability Q of having a value of $\chi^2 \geq \chi^2_{observed}$ for a source assumed to have constant flux, and then defined the variability index $V = -\log Q$. Sources with $V < 0.5$ were classified as *non-variable*, with $0.5 \leq V < 1$ as *uncertain*, and with $V \geq 1$ as *variable*. A high V may indicate either strong flux variations or weak flux variations detected with small flux errors. Moreover, sources with a very small number of detections may also have low V (Nolan et al. 2003). We computed a second version of the variability index, $V_{sys3\sigma}$, by adding a 10% systematic component to each of the flux errors, where the 10% figure is based on Monte Carlo simulations, pre-flight beam tests and in-flight analysis of known sources. Finally, we computed a third version, $V_{sys2\sigma}$, of the V parameter as $V_{sys3\sigma}$, which also included the flux measures with $2 \leq \sqrt{TS} \leq 3$, for which the ALIKE task produces a 95% c.l. flux upper limit (UL). In this case we set the flux errors to $(F_{UL} - F_i)/2$. The two indices, $V_{sys3\sigma}$ and $V_{sys2\sigma}$, which take systematic errors into account, will tend to be lower than V , which takes into account only the statistical error. These indices serve as the reference ones in our variability analysis, where $V_{sys2\sigma}$ allows a larger detections sample for each source to provide some variability information for sources with few pointings. We excluded from the calculation of the indices the detections with a mean effective exposure lower than $9 \times 10^6 \text{ cm}^2\text{s}$, corresponding to a small number of detections in OBs with a few days duration executed during the verification phase (July–November 2007).

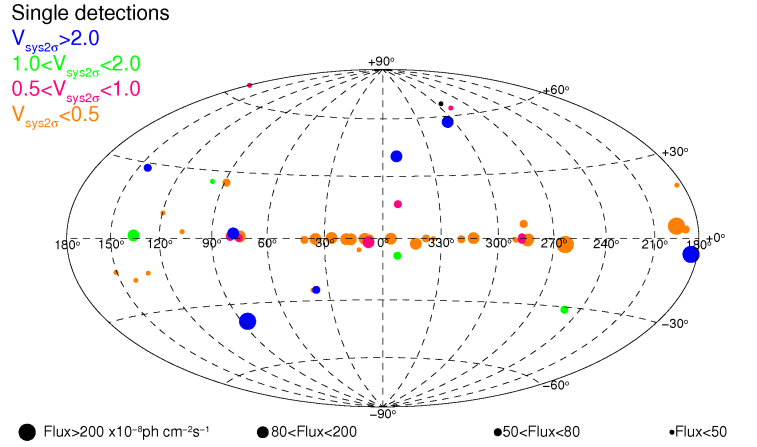


Fig. 3. Aitoff projection of the 54 distinct source positions detected on all pointed observations data (symbol colors indicate the variability parameter $V_{sys2\sigma}$ of the 53 sources for which we define with blue the highest and with orange the lowest value. 1AGL J1238+0406 has a single detection and so is marked in black. Marker sizes are proportional to flux).

We calculated a fourth variability index, F_{sys} , similar to that used in the Fermi catalogues (Abdo et al. 2009; Abdo et al. 2010a), defined as a χ^2 again including a 10% systematic error in the weights, to directly compare it with the Fermi 1FGL index. In our analysis each source has a different number of detections (N_{det}) and so this parameter is expected to behave as the χ^2_n distribution where the number of degrees of freedom (dof) is $n = N_{det} - 1$. For this reason we considered the *reduced* F_{sys} ($Reduc.F_{sys} = F_{sys}/N_{dof}$), and compared it with the 1FGL variability index divided by 10 (i.e. the number of dof in 1FGL), and similarly with the 2FGL variability index divided by 23. We discuss in Section 7 a possible comparison with the 2FGL index as well, which is instead based on an ML ratio test statistic.

6. Results: the catalogue and source variability

Applying our selection criteria, we obtained a sample of 54 distinct sources (Fig. 3) with a total of 1209 OB detections. Eight 1AGL sources (2 high latitude and 6 on the galactic plane) were not detected in this processing either because of the low OB exposures and/or due to specific complex Galactic regions. We show information about the mean flux of these sources in Table 3, as obtained in the 1AGL.

We describe in the following the variability results (listed in Table 4) and the light curves of bright pulsars and of some prominent sources. We compared the light curves of sources with a known counterpart with those in the most recent Fermi catalogue (Nolan et al. 2012) for the time period common to both catalogues. The non-uniform exposures among the OBs together with the pointing strategy put strong constraints on the variability analysis.

The source and detections table⁵, Table 5, includes all the source flux measurements with $\sqrt{TS} \geq 2$ obtained for each of the 54 sources detected in this processing. In Table 5 we report the main parameters of the maximum \sqrt{TS} detection for each source. These are the name, coordinates, the \sqrt{TS} , the $E > 100$ MeV flux, the four variability indices described above and the

⁵ Available on-line at <http://www.asdc.asi.it/agile1rcat>

Source name	R.A. (J2000.0) (hh mm ss)	Dec. (J2000.0) (dd mm ss)	LII,BII (deg,deg)	Error Rad. (deg)	Mean Flux \pm Error ($\times 10^{-7}$ ph cm $^{-2}$ s $^{-1}$)
1AGL J0657+4554	06 57 29.2	+45 54 14.5	170.73 , 20.11	0.55	3.1 \pm 0.6
1AGL J1043-5749	10 43 56.0	-57 49 51.0	286.60 , 0.94	0.68	2.2 \pm 0.5
1AGL J1222+2851	12 22 39.7	+28 51 02.3	196.09 , 83.42	0.74	3.8 \pm 1.1
1AGL J1412-6150	14 12 06.1	-61 49 32.5	312.30 , -0.43	0.44	4.3 \pm 0.7
1AGL J1746-3017	17 46 01.5	-30 17 23.7	358.89 , -0.78	0.68	6.6 \pm 1.6
1AGL J1815-1732	18 15 29.7	-17 32 27.1	13.29 , -0.28	0.65	5.2 \pm 1.3
1AGL J1901+0430	19 01 20.8	+04 29 38.5	38.06 , -0.15	0.58	4.5 \pm 1.1
1AGL J1923+1404	19 22 53.7	+14 03 45.2	49.00 , -0.42	0.64	6.0 \pm 1.0

Table 3. 1AGL sources not detected in this analysis. The information is taken from 1AGL, meaning these are first-year data.

number of detections, the confirmed counterparts and source class, if any, and other possible associations ordered according to the distance from the AGL source. We used the abbreviation *1AGLR* for new sources and repositioned 1AGLs.

Below this row a list with all the flux measurements in each OB is shown with the observation parameters MJD start/stop, the OB number, the OB \sqrt{TS} , the $E > 100$ MeV flux or the ULs for $2 \leq \sqrt{TS} \leq 3$, and the off-axis angle. The flux errors are statistical only, i.e. the results of our analysis. The association column is populated with sources from well-known catalogues that fall within error circles of radii given by the 95% statistical plus the 0.1° systematic, linearly added. In particular, sources from the 1AGL were the first included when present, then sources from the BZCAT (Massaro et al. 2008), from 3EG and 2FGL. Associations from known radio (Rinsland et al. 1975; Gregory et al. 1996), TeV (TEVCAT⁶), SNR (Green 2009), PSR (Manchester et al. 2003), and HMXB (Liu et al. 2006) catalogues were included for some sources without a previously confirmed counterpart (TeV emitting PWNs associated with bright pulsars are not shown).

6.1. Variability results

The V index distributions are given in Fig. 4. They show that V values peak in the non-variable–uncertain ranges for all indices and that the V distribution is on average lower than the $V_{sys2\sigma}$ (average values for V and $V_{sys2\sigma}$ are 3.6 and 1.8), because of the obviously higher number of detections used for the $V_{sys2\sigma}$. The $V_{sys2\sigma}$ and $Reduc.F_{sys}$ gave similar results, as expected (Fig. 4), with a correlation factor 0.84. We then used this correlation to estimate a variability threshold for $Reduc.F_{sys}$ extrapolated from the $V_{sys2\sigma}$ threshold, considering the approximate intersection of the $V_{sys2\sigma} = 1$ line with the linear correlation plot. We estimated two possible linear correlation whose steepest and faintest slope included all points, obtaining a range of the $Reduc.F_{sys}$ values at the intersection of 1.55–1.65, so we chose as threshold $Reduc.F_{sys} \approx 1.6$. Details on the variability results obtained for different source classes are given in Table 4, for which we consider only sources with confirmed counterparts, except for 9 high-latitude sources associated with well known blazars also included as AGNs. The majority of variable sources are blazars according to all indices, the most variable one is 3C 454.3. The fraction of variable

sources according to the $V_{sys2\sigma}$ index is 20%, and a similar result, 22%, is obtained according to $V_{sys3\sigma}$.

Variability Type	Number of Sources ($V, V_{sys3\sigma}, V_{sys2\sigma}$)	Source class: Number of variables
Variable	13, 12, 11	AGN:7,8,8; PSR:1,0,0; PSR*:1,1,1;HMXB:1,1,1; CWB:1,0,0;SNR:0,0,0; Unidentified:2,2,1
Uncertain	8, 5, 8	AGN:2,1,3;PSR:3,2,1; HMXB:1,0,1;SNR:0,0,0; CWB:0,1,1;Unidentified:2,1,2
Non-variable	21, 25, 34	AGN:7,7,6; PSR:4,6,8; HMXB:0,1,0;SNR:2,2,2; CWB:0,0,0;Unidentified:8,9,18

Table 4. Variability analysis results according to the V , $V_{sys3\sigma}$, and $V_{sys2\sigma}$ indices, divided in to six main source classes. The last column lists the number of sources of each variability type found in each source class according to each index, in the same order as in the second column. The PSR* source is the Crab pulsar + nebula.

However, the F_{sys} parameter and consequently V (which is based on the calculation of the χ^2), depend on the ratio between mean flux and the standard deviation, so it is expected to be more likely to classify faint sources (flux $< 3.0 \times 10^{-7}$ ph cm $^{-2}$ s $^{-1}$) or those near the Galactic plane as non-variable. Most of the unclassified sources are non-variable, but about half of the unclassified have an unconfirmed association with 2FGL pulsars.

6.2. Light curves of bright pulsars

The light curves of the Vela and Geminga pulsars are shown in Figs. 5 and 6, and that of the Crab pulsar + nebula in Fig. 7. Vela and Geminga are the brightest among the non-variable sources. In all figures the mean off-axis angles and the \sqrt{TS} in each OB are shown as well.

The weighted mean of the OB Vela fluxes is $86.8 \pm 1.0 \times 10^{-7}$ ph cm $^{-2}$ s $^{-1}$ while the value from the updated deep

⁶ <http://tevcat.uchicago.edu>

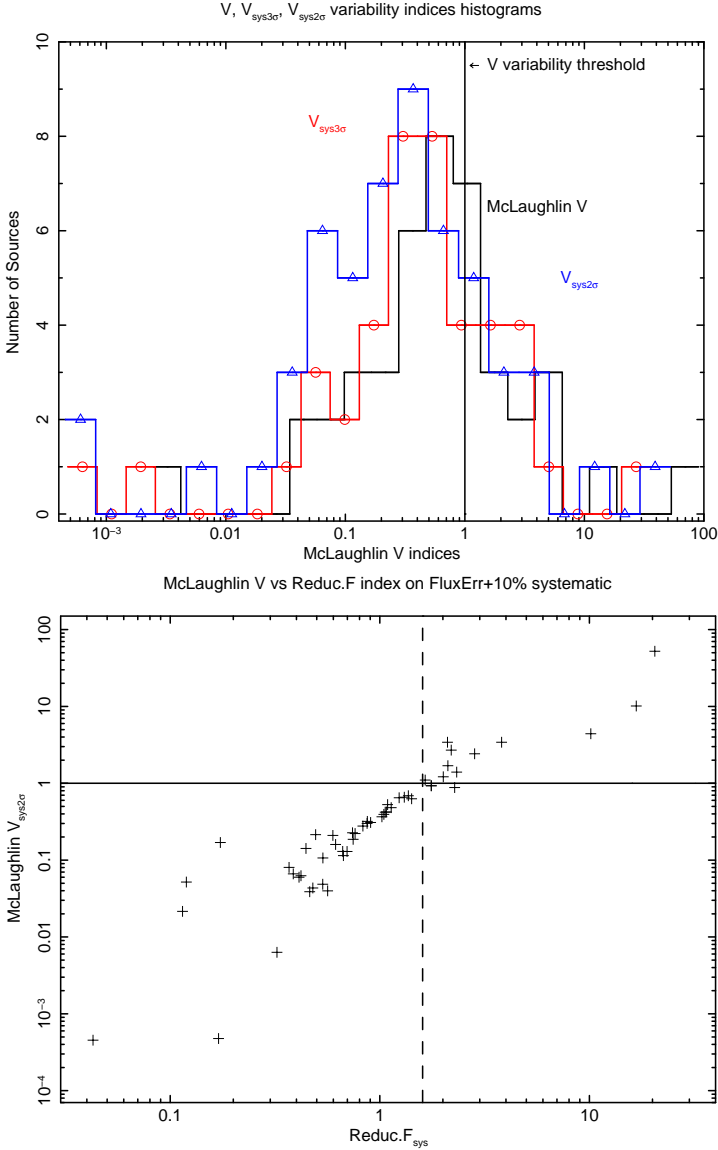


Fig. 4. Upper panel: histograms of the V (black unmarked line), $V_{\text{sys}2\sigma}$ (red line with circles), and $V_{\text{sys}3\sigma}$ (blue lines with triangles) parameters; lower panel: plot of $V_{\text{sys}2\sigma}$ vs the $\text{Reduc.}F_{\text{sys}}$. The vertical line in the upper plot is the threshold above which a source is variable ($V \geq 1$) according to the V parameters. The horizontal line in the lower plot has the same meaning, while the vertical dashed line is the approximated extrapolation of a threshold for source variability for the $\text{Reduc.}F_{\text{sys}}$ parameter, taking into account the correlation of both parameters.

maps is $88.2 \pm 0.9 \times 10^{-7} \text{ ph cm}^{-2} \text{ s}^{-1}$, which is $\sim 3.2\sigma$ higher than the mean value from the first AGILE catalogue, $78.0 \pm 3.2 \times 10^{-7} \text{ ph cm}^{-2} \text{ s}^{-1}$, according to the 1AGL error. We did not overplot the new mean value estimated from deep maps because the variability study is based on the mean of the OB fluxes. This new value, which should be considered as the new reference one, is higher than the previous value primarily because of the new instrument response functions, which compensate for the effect of energy dispersion, as well as the new filter calibrated up to a high off-axis angle. We obtained $V_{\text{sys}2\sigma} = 0$ and $F_{\text{sys}} = 1.87$, with 13 dof and expect a constant source to produce a value of $F_{\text{sys}} \leq 2.1$ at 99% c.l.

A particular case is that of the Crab Nebula, which has recently been discovered to be a variable γ -ray source (see Tavani et al. 2011a, 2011b, Abdo et al. 2011). In Fig. 6, first panel,

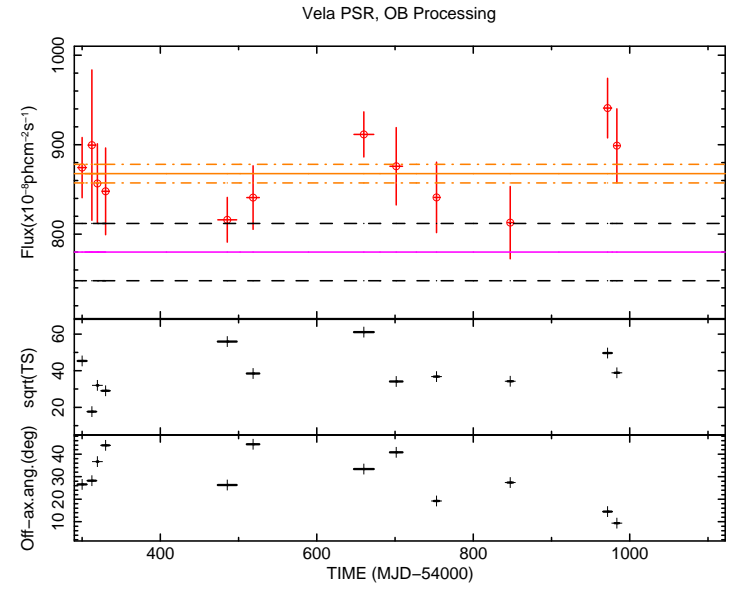


Fig. 5. Vela pulsar $E > 100 \text{ MeV}$ light curve in $10^{-8} \text{ ph cm}^{-2} \text{ s}^{-1}$ (upper panel), the \sqrt{TS} (middle panel), and the off-axis angle (in degrees) as a function of time in MJD (lower panel). The 1AGL flux value and the 1σ error levels are shown as a magenta line and black dashed lines, while the weighted mean value of all OBs and its 1σ error levels are shown in orange.

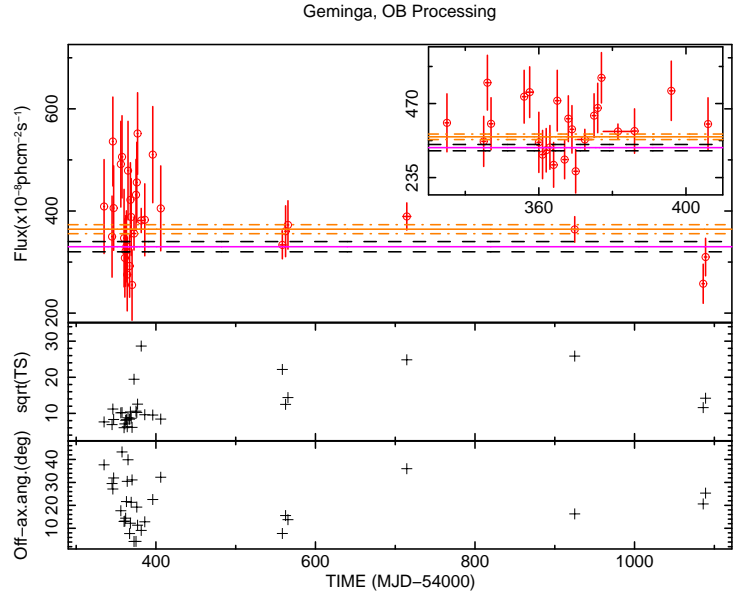


Fig. 6. Geminga pulsar $E > 100 \text{ MeV}$ light curve in $10^{-8} \text{ ph cm}^{-2} \text{ s}^{-1}$ (upper panel), the \sqrt{TS} (middle panel), and the off-axis angle (in degrees) as a function of time in MJD (lower panel) for detections with an off-axis angle lower than 50° and exposures greater than $9 \times 10^6 \text{ cm}^2 \text{ s}$. The 1AGL flux value and the 1σ error levels are shown as magenta line and black dashed lines, while the weighted mean flux and its 1σ error levels are shown in orange (solid and dash-dotted lines).

we plot the Geminga light curve and its weighted mean OB flux value, $36.4 \pm 0.9 \times 10^{-7} \text{ ph cm}^{-2} \text{ s}^{-1}$, is shown. In Fig. 7 the Crab light curve shows the October 2007 flaring episode (MJD=54381.5, OB 4200), discussed in Tavani et al. (2011b), at a higher flux than for the 2010 flare. The Crab (Nebula + PSR) weighted mean OB flux value, $23.2 \pm 0.9 \times 10^{-7} \text{ ph cm}^{-2} \text{ s}^{-1}$, was

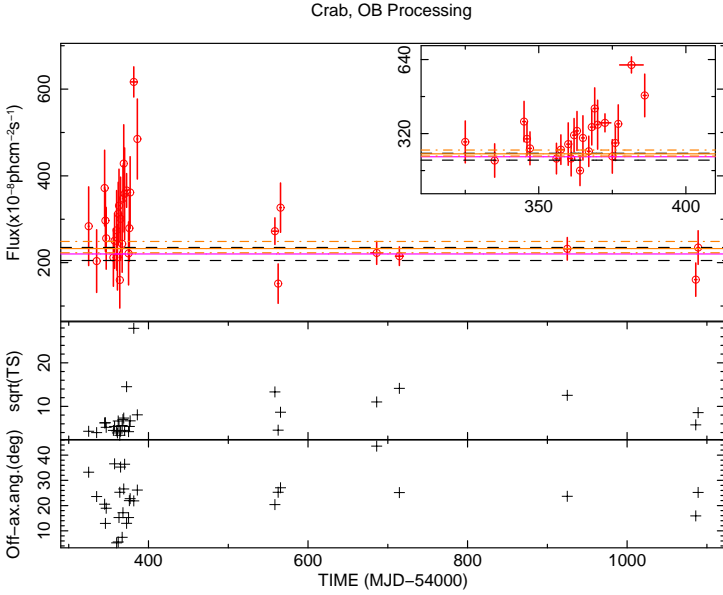


Fig. 7. Crab $E > 100$ MeV light curve (upper panel), the \sqrt{TS} (middle panel), and the off-axis angle (in degrees) as a function of time (lower panel) for detections with an off-axis angle lower than 50° and exposures greater than 9×10^6 cm 2 s. The 1AGL flux values and the 1σ error levels are shown as magenta line and black dashed lines, while the weighted mean value of all OB fluxes and its 1σ error levels are shown in orange. The 2007 Crab flare episode (MJD=54381.5) is its most significant detection at a flux of $62.0 \pm 7.0 \times 10^{-7}$ ph cm $^{-2}$ s $^{-1}$. Large error bars at MJD ≤ 54420 are mostly obtained with 1-3 day exposures.

calculated excluding seven OB during the 2007 flare (in the interval 54368–54396). We obtained $V_{sys2\sigma} = 0.4$ for Geminga and $V_{sys2\sigma} = 3.4$ for Crab. If we remove the 2007 flare peak from the Crab light curve we obtain $V_{sys2\sigma} = 0.8$, while if we remove all seven OB that cover the flare period that was excluded for the mean value estimate, we obtain $V_{sys2\sigma} = 0.1$, a non-variable value.

6.3. Long-term light curves of some prominent sources

We report here four long-term light curves, in the $E > 100$ MeV band, obtained for sources classified as variable, non-variable and a particular case of an uncertain one. We show in Figs. 8 and 9 the results for the two known blazars 3C 454.3 and PKS 1830-211. Light curves are shown including source detections with flux errors at 1σ , not including any systematic error.

Fig. 8 shows the strong variability in the 3C454.3 flux even at the OB time scale, and in particular the decreasing trend reported in Vercellone et al. (2010). This source has the strongest variability index $V_{sys2\sigma} = 52.3$. This confirms what was expected in Vercellone et al. (2004), a study of EGRET blazar activity and duty-cycle evaluation, which was based on a differently defined variability index.

1AGLR J1833-2057, associated to PKS 1830-211, is instead one of the fifteen new sources not included in 1AGL. Its light curve shows a detection in the period of the October 2009 flare (Striani et al. 2009), with a flux of $(3.2 \pm 0.8) \times 10^{-7}$ ph cm $^{-2}$ s $^{-1}$, compatible with the one-week average flux (4.0×10^{-7} ph cm $^{-2}$ s $^{-1}$) reported in Donnarumma et al. (2011), based on data of the OB 8300 only, and shown to be three times weaker than the peak flare flux. This source is classified as non-variable according to all parameters, however, because of the flux averaging over the OB time scale. Other detec-

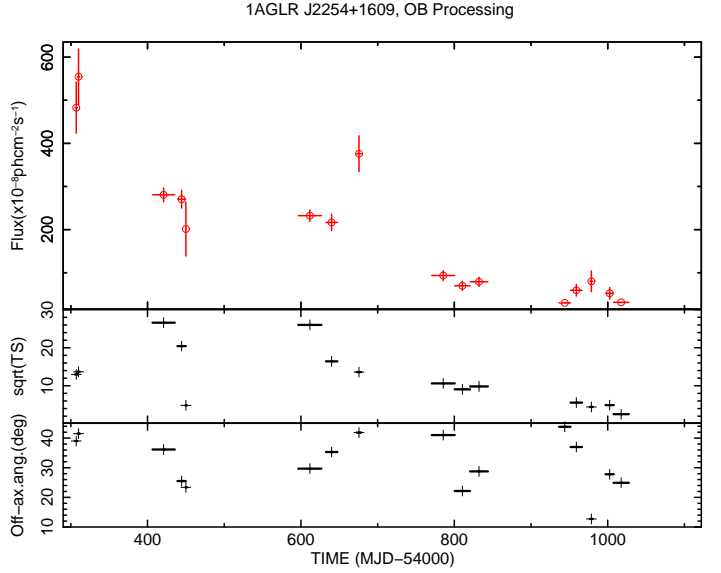


Fig. 8. 3C 454.3 $E > 100$ MeV light curve in 10^{-8} ph cm $^{-2}$ s $^{-1}$ (upper panel), the \sqrt{TS} (middle panel), and off-axis angle (in degrees) as a function of time in MJD (lower panel).

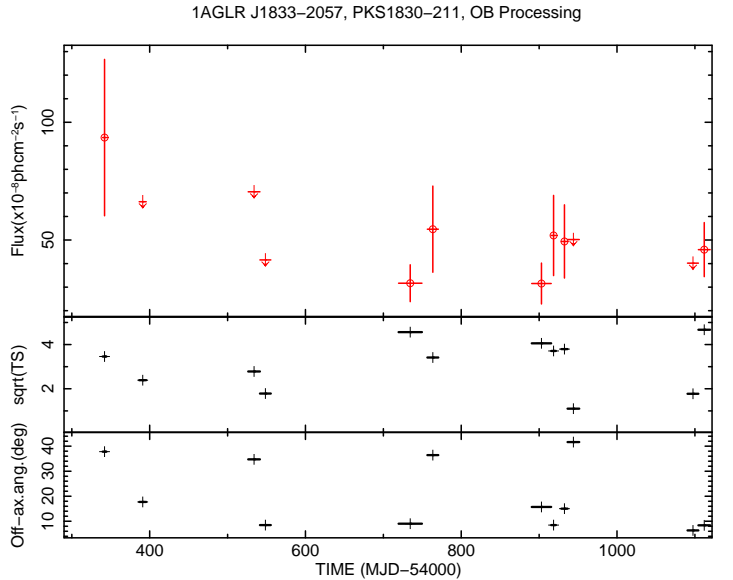


Fig. 9. 1AGLR J1833-2057/PKS 1830-211 $E > 100$ MeV light curve in 10^{-8} ph cm $^{-2}$ s $^{-1}$ (upper panel), the \sqrt{TS} (middle panel), and the off-axis angle (in degrees) as a function of time in MJD (lower panel).

tions have been obtained, the most significant one in September 2008. This detection showed some source activity one year before the October 2009 flare, with a time scale between the two events similar to that between the 2009 and the following 2010 flare, which was also detected by Fermi (see discussion in Donnarumma et al. 2011).

In Fig. 10 we show the 1AGLR J2021+4030 light curve, a source that falls in the γ Cygni SNR region. The 1AGLR J2021+4030 variability on six-day time scale on pointing data (up to August 2009) was extensively discussed in Chen et al. (2011a), where values of 3.88 and 2.18 in $E > 100$ MeV were found for V and $V_{sys2\sigma}$, respectively, while low variability was detected at $E > 400$ MeV. The corresponding values in this pa-

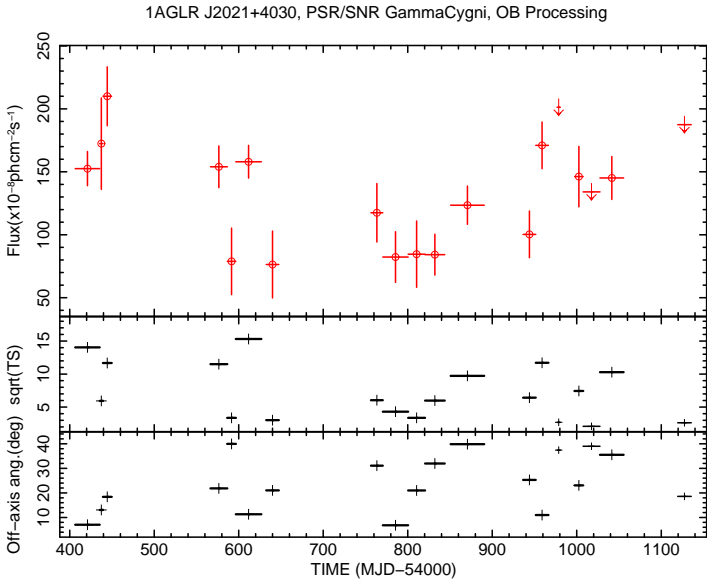


Fig. 10. 1AGLR J2021+4030 $E > 100$ MeV light curve in 10^{-8} $\text{ph cm}^{-2} \text{s}^{-1}$ (upper panel), the \sqrt{TS} (middle panel), and the off-axis angle (in degrees) as a function of time in MJD (lower panel).

per are 5.9 and 2.70 and the light curve is compatible with that therein. 1AGLR J2021+4030 field is complex and there could be contribution to the variability from other γ -ray sources, that are possibly transient, in addition to LAT PSR J2021+4026 (see Chen et al. 2011a, for more details).

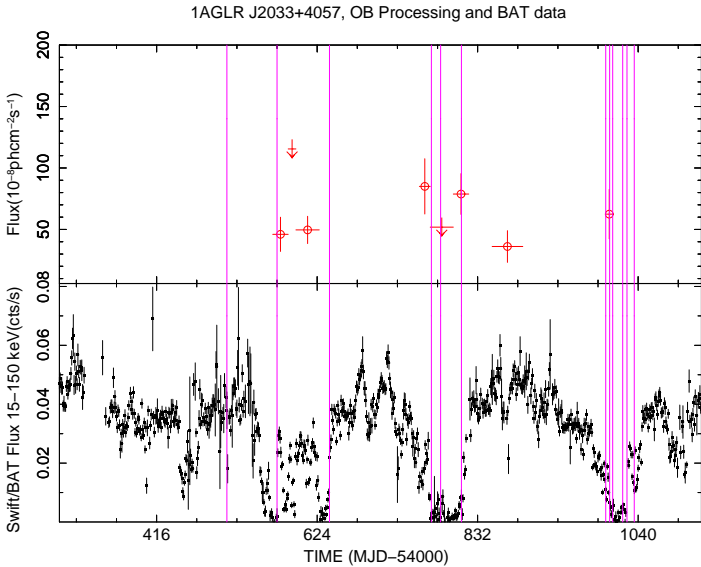


Fig. 11. 1AGLR J2033+4057/Cyg X-3 $E > 100$ MeV light curve (upper panel) compared with the Swift/BAT $15 < E < 150$ keV daily light curve. The plot shows six detections with $\sqrt{TS} > 3$. The 1–2 days γ -ray flare times described in Tavani et al. (2009c), Bulgarelli et al. (2012a), and Piano et al. (2012) are marked with vertical magenta lines. For some lines there is no corresponding UL when they have $\sqrt{TS} < 2$.

Finally, we show in Fig. 11 the 1AGLR J2033+4057/Cyg X-3 light curve together with the 15–150 keV daily light curve from Swift/BAT (Barthelmy et al. 2005). This plot is similar to those reported in Tavani et al. (2009c), Bulgarelli et al. (2012a), and Piano et al. (2012). Here we show the 1–2-day γ -ray flare

times in the Pointing mode interval described there. Our detections correspond to the reported activity periods, and moreover a flux UL at $\sqrt{TS} = 2.7$ (MJD=54591.5) is compatible with a short *dip* in the BAT hard X-ray light curve. We performed an additional ML analysis on a three-day time scale that found an additional low-significance ($\sqrt{TS} = 4$) short time scale γ -ray emission enhancement not included in Piano et al. (2012), which in fact reported the γ -ray activity on the 1–2-day time scale. Again our flux variations are averaged on longer time intervals, so that this source is only classified as uncertain in this analysis.

7. Discussion and conclusions

We reported the results of a variability analysis in the $E > 100$ MeV band of a catalogue of 54 sources obtained as an update of the 1AGL using the complete AGILE pointing mode OB archive. The new source list includes seven previously undetected sources with AGN counterparts and eight at low latitudes, while eight 1AGL sources were not detected in this analysis, two of which are at high latitude (1AGL J0657+4554 and 1AGL J1223+2851/WComae) and six are on the Galactic plane (1AGL J1044-5750, 1AGL J1412-6150, 1AGL J1746-3017, 1AGL J1815-1732, 1AGL J1901+0430, 1AGL J1923+1404).

We carried out the variability study by applying an ML analysis in each single OB without implementing any blind search for transient sources, among OBs with different exposure times.

This ML variability analysis, as discussed in Section 5, is known to be inadequate for the variability indices used (Nolan et al. 2003); however, the revised indices allowed us to distinguish variable from non-variable sources. All four variability indices defined in our analysis show that the majority of variable sources are blazars, consistent with the γ -ray source variability studies included in the first (1FGL) and second (2FGL) Fermi source catalogues.

A comparison with the 1FGL and 2FGL variability indices is shown in Fig. 12. The index from the 1FGL is a χ^2 statistic calculated in the same manner as F_{sys} , while the 2FGL statistic is an ML ratio test statistic, defined in Nolan et al. (2012), which is distributed according to the χ^2_{23} distribution in the null hypothesis of a constant source.

We associated our source list with those of 1FGL and 2FGL by a simple spatial cross-matching with radius $30'$, yielding 46 and 49 sources in common, respectively. We used the $\text{Reduc.}F_{\text{sys}}$ parameter because each source is detected in a different number of OBs (see Section 5).

For each source we defined a specific threshold for flux variability at 99% c.l. (as in Abdo et al. 2010a; Nolan et al. 2012) using the appropriate χ^2_n distribution for n dof. Thresholds range from 1.67 for a source with 31 detections to 6.2 for one with two detections, while the 1FGL and 2FGL thresholds are 2.32 and 1.81, respectively. Twelve sources out of 54 have fewer than five detections. Sources with a $\text{Reduc.}F_{\text{sys}}$ higher than their own threshold ($\text{Reduc.}F_{\text{sys}} > \chi^2_{\text{thres}}/N_{\text{dof}}$) are flagged as variable in the plot. We found that all of the AGILE variable sources, seven sources, are also variable in 1FGL except for two, the Crab and 1AGLR J2021+4030, while in 2FGL only 1AGLR J2021+4030 remains non-variable. The Crab case is clear: the AGILE pointing dataset included the very intense 2007 flare, with a peak flux three times the 1AGL mean flux, whose evolution is shown in various consecutive short-duration OBs (see Table 1), while fewer pointings are available from 2008 on. 1FGL included a flare affecting only the last of the 11 bins in the catalogue, while the 2FGL results show a much higher variability than for a lower

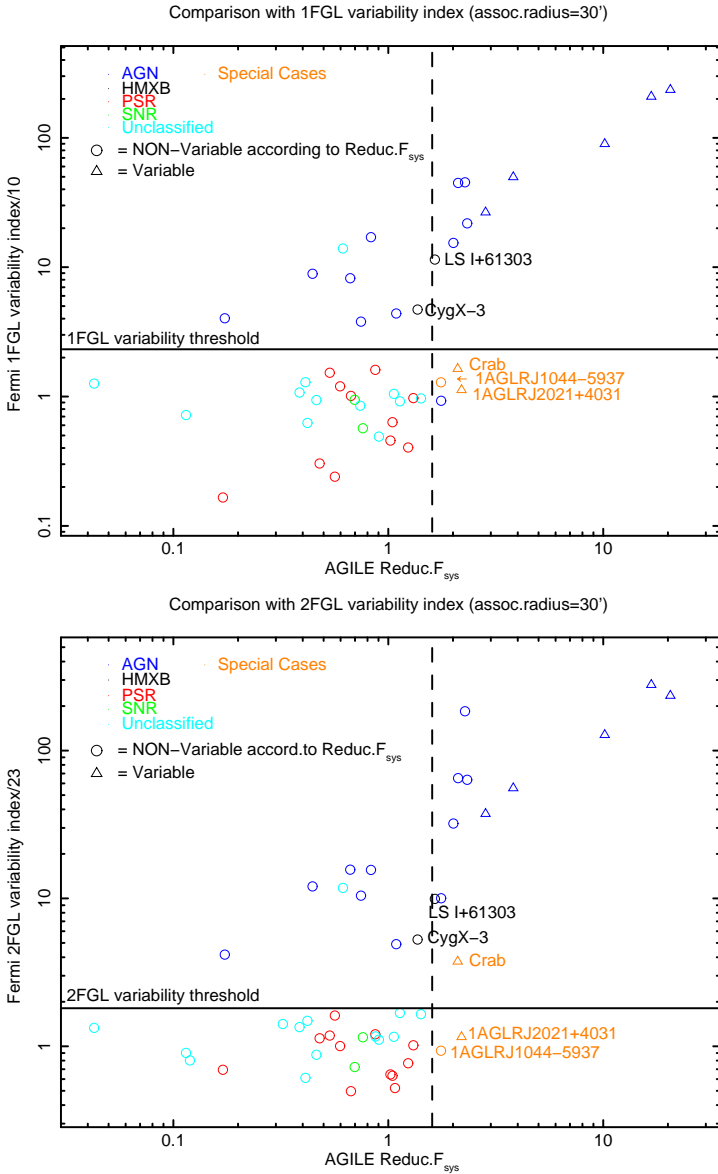


Fig. 12. Upper plot: Fermi 1FGL variability index divided by 10 vs $Reduc.F_{sys}$ for all detections associated with the 1FGL sources with a cross-matching with radius $30'$, where colours correspond to source classes, blue for AGNs, black for HMXBs, red for PSRs, green for SNRs, light-blue for the unclassified ones, and orange for the three *Special Cases* Crab nebula + pulsar, 1AGLR J2021+4030 (γ Cygni region) and 1AGLR J1044-5944 (Eta Carinae). Markers correspond to AGILE variability type according to $Reduc.F_{sys}$, i.e. circles for non-variable and triangles for variable. The lower plot is obtained with association to the 2FGL catalogue with the same radius and shows the 2FGL index divided by 23. The black horizontal lines are the 1FGL and 2FGL variability thresholds, 2.32 and 1.81, while the dashed vertical lines correspond to the approximately extrapolated threshold (1.6) for the AGILE variability $Reduc.F_{sys}$ parameter obtained from the correlation with the $V_{sys2\sigma}$ parameter.

mean flux with a smaller error. As discussed in Section 6.3, the variable emission from 1AGLR J2021+4030 might be generated by the contribution from other sources apart from the pulsar.

Sources in the plots are divided into five main classes: AGN, PSRs, HMXBs, SNRs, and unclassified sources, while three particular cases are labelled separately (Crab PSR + nebula, 1AGLR J2021+4030 and 1AGLR J1044-5944). Only sources with confirmed (based on 1AGL and later AGILE results) coun-

terparts were included in the specific classes, except for 9 high-latitude sources associated to well known blazar counterparts included as AGNs.

A good correlation with the 1FGL parameter is obtained for AGN whose diffuse γ -ray background is low, with a correlation factor of 0.98, which is expected for this class, taking into account their broad flux distribution and that at low fluxes ($\leq 3.0 \times 10^{-7}$ ph cm $^{-2}$ s $^{-1}$ for a typical AGN variability of 1-3 days) AGILE cannot detect variability. Lower correlation factors are obtained for PSRs and unclassified (0.01 and 0.05). The correlation factor considering all sources together is 0.98. The PSRs are all non-variable except for the two particular cases discussed above.

Lower values were also obtained for the correlation of $Reduc.F_{sys}$ with the 2FGL index (0.88 for AGN, -0.28, 0.08 for PSRs and unclassified, while the value including all sources is 0.89), for AGN due also to 3C 273, whose variability index increased by a factor 4 from 1FGL to 2FGL (excluding it, the correlation factor for AGN is 0.97) and to 1AGLR J1625-2531 which became variable in 2FGL with an increase of a factor 10 in the variability index. We note the presence of an unclassified source within the AGN group in both plots. This is 1AGLR J2016+3644, a source within the Cygnus region that is non-variable according to $Reduc.F_{sys}$ (and also $V_{sys2\sigma} = 0.2$), whose nearest Fermi sources are the unclassified 1FGL J2015.7+3708 (at $25'$), 2FGL J2015.6+3709/MG2 J201534+3710 (at $27'$), classified as a blazar of uncertain type, 2FGL J2018.0+3626 (unassociated, at $27'$) and the SNR G74.9+1.2 ($28'$). All sources are slightly outside the 1AGLR J2016+3644 error circle, however. The comparison with the vertical dashed lines, the threshold at 1.6, shows that some sources marked with circles could be variable according to $V_{sys2\sigma}$, as confirmed by the exact numbers in Table 4. For instance, eight AGNs are variables according to $V_{sys2\sigma}$ and ten blue points are rightward of the dashed line, while there are only five triangles.

The inhomogeneous exposure times among the OBs diminish the capability of studying the source variability in our data analysis; for this reason a similar analysis on the one-week time scale on the same pointing data archive would be useful to better classify the source variability, and will be reported in a future work.

Acknowledgements. The AGILE Mission is funded by the Italian Space Agency (ASI) with scientific and programmatic participation by the Italian Institute of Astrophysics (INAF) and the Italian Institute of Nuclear Physics (INFN). Research partially supported through the ASI grants I/089/06/2, I/042/10/0 and I/028/12/0. The authors thank the anonymous referee for the useful suggestions.

References

- Abdo, A.A., Ackermann, M., Atwood, W.B., et al., 2008, *Science*, Vol. 322, no. 5905, 1218
- Abdo, A.A., Ackermann, M., Ajello, M., et al., 2009, *ApJS*, 183, 46
- Abdo, A.A., Ackermann, M., Ajello, M., et al., 2010a, *ApJ*, 715, 429
- Abdo, A.A., Ackermann, M., Ajello, M., et al., 2010b, *Science*, 329, 817
- Abdo, A.A., Ackermann, M., Ajello, M., et al., 2011, *Science*, 331, 739
- Atwood, W.B., Abdo, A.A., Ackermann, M., et al., 2009, *ApJ*, 697, 1071
- Barbiellini, G., Bordignon, G., Fedel, G., et al., 2001, *AIP Conf. Proc.* 587, 754
- Barbiellini, G., Fedel, G., Liello, F., et al., 2002, *NIM A*, 490, 146
- Barthelmy, S.D., Barbier, L.M., Cummings, J.R., et al., 2005, *Space Science Reviews*, 120, 143
- Bulgarelli, A., Trifoglio, M., Gianotti, F., et al., 2008, *Proceedings of Astronomical Data Analysis Software and Systems XVIII*, Quebec, Canada, ADASS, ASP Conference Series
- Bulgarelli, A., Chen, A., Giuliani, A., et al., 2009, *GRID Scientific Analysis User Manual*, AGILE-IFC-OP-009
- Bulgarelli, A., Argan, A., Barbiellini, et al., 2010, *NIM A*, 614, 213
- Bulgarelli, A., Tavani, M., Chen, A., et al., 2012a, *A&A*, 538, A63

- Bulgarelli, A., Chen, A., Tavani, M., et al., 2012b, *A&A*, 540, A79
 Cattaneo, P.W., Argan, A., Boffelli, F., et al., 2011, *NIM A*, 630, 251
 Cattaneo, P.W., Rappoldi, A., Argan, A., et al., 2012, *SPIE*, Vol. 8443E, 4D
 Chen, A., Piano, G., Tavani, M., et al., 2011a, *A&A*, 525A, 33
 Chen, A., Bulgarelli, A., Contessi, T., et al., 2011b, *GRID Scientific Analysis User Manual*, AGILE-IFC-OP-009_Build-21, (available on-line at <http://agile.asdc.asi.it/publicsoftware.html>)
 Chen, A., Argan, A., Bulgarelli, A., et al., 2012, *SPIE*, Vol. 8443E, 4E
 Chen, A., Argan, A., Bulgarelli, A., et al., 2013, *A&A*, submitted
 Dame, T.M., Hartmann, D., Thaddeus, P., 2001, *ApJ*, 547, Issue 2, 792
 Donnarumma, I., De Rosa, A., Vittorini, V., et al., 2011, *ApJ*, 736, L30
 Feroci, M., Costa, E., Soffitta, P., et al., 2007, *NIM A*, 581, 728
 Giuliani, A., Chen, S., Mereghetti, et al., 2004, *Mem. SAIt Suppl.*, 5, 135
 Giuliani, A., Cocco, V., Mereghetti, S., Pittori, C. and Tavani, M., 2006, *NIM A*, 568, 692
 Giuliani, A., Tavani, M., Bulgarelli, A., et al., 2010, *A&A*, 516, L11
 Green, D.A., 2009, *BASI*, 37, 45.
 Gregory, P.C., Scott, W.K., Douglas, K.; Condon, J.J., 1996, *ApJS*, 103, 427
 Hartman, R. C., Bertsch, D.L., Bloom, S.D.; Chen, A.W., et al., 1999, *ApJS*, 123, 79H
 Kalberla, P.M.W., Burton, W.B., Hartmann, D., et al., 2005 *A&A* 440, Issue 2, pp.775-782
 Labanti, C., Marisaldi, M., Fuschino, F., et al., 2006, *SPIE*, Vol. 6266, 62663Q
 Labanti, C., Marisaldi, M., Fuschino, F., et al., 2009, *NIM A*, 598, 470
 Liu, Q.Z., van Paradijs, J., van den Heuvel, E.P.J., 2006, *A&A*, 455, 1165
 Manchester, R.N., Hobbs, A.T., Hobbs, M., 2005, *AJ*, 129, 1993-2006 (2005)
 Massaro, E., Giommi, P., Leto, L., et al., 2008, [arXiv:0810.2206], (on-line interactive table available at <http://www.asdc.asi.it/bzcat>)
 Mattox, J.R., Bertsch, D.L., Chiang, J., et al., 1996, *ApJ*, 461, 396
 McLaughlin, M.A., Mattox, J.R., Cordes, J.M., Thompson, D.J., 1996, *ApJ*, 473, 763
 Michelson, P.F., 2008, *APS Meeting Abstracts*, TSSP, L2002
 Morselli, A., Argan, A., Barbiellini, G., et al., 2013, *NUPH B*, in press
 Nolan, P.L., Abdo, A.A., Ackermann, M., et al., 2012, *ApJS*, 199, 31
 Nolan, P.L., Tompkins, W.F., Grenier, I.A., et al., 2003, *ApJ*, 597, 615
 Rinsland, C., Dixon, R., Kraus, J., 1975, *AJ*, 80, 759
 Paredes, J.M., Mart, J., Torres, D.F., 2005, *Ap&SS*, 297, 223
 Perotti, F., Fiorini, M., Incorvaia, S., Mattaini, E., & Sant’Ambrogio, E., 2006, *NIM A*, 556, 228
 Piano, G., Tavani, M., Vittorini, V., et al., 2012, *A&A*, 545, A110
 Pittori, C., and Tavani, M., 2002, *NIM A*, 488, 295
 Pittori, C., Verrecchia, F., Chen, A.W., et al., 2009, *A&A*, 506, 1563
 Prest, M., Barbiellini, G., Bordignon, G., et al., 2003, *NIM A*, 501, 280
 Romero, G.E., Benaglia, P., Torres, D.F., et al., 1999, *A&A*, 348, 868
 Sabatini S., Tavani, M., Striani, E., et al., 2010, *ApJ*, 712, 10
 Striani, E., et al., *ATel*, 2242, 1
 Tavani, M., Barbiellini, G., Argan, A., et al., for the AGILE Collaboration, 2008, *NIM A*, 588, 52 [arXiv:0807.4254]
 Tavani, M., Barbiellini, G., Argan, A., et al., for the AGILE Collaboration, 2009a, *A&A*, 502, 995
 Tavani, M., Sabatini, S., Pian, E., et al., 2009b, *ApJ*, 698, L142
 Tavani, M., Bulgarelli, A., Piano, G., et al., 2009c, *Natur*, 462, 620
 Tavani, M., Giuliani, A., Chen, A.W., et al., 2010, *ApJ*, 710, L151
 Tavani, M., 2011a, *AAS*, 217, 43406
 Tavani, M., Bulgarelli, A., Vittorini, V., et al., 2011b, *Science*, 331, 736 [arXiv:1101.2311]
 Thompson, D.J., Bertsch, D.L., Fichtel, C.E., et al., 1993, *ApJS*, 86, 629
 Thompson, D.J., 2008, *RPPh*, 71k, 6901
 Torres, D.F., Romero, G.E., Combi, J.A., et al., 2001, *A&A*, 370, 468
 Trifoglio, M., Bulgarelli, A., Gianotti, F. et al., 2008, *Proceedings of SPIE*, Vol. 7011, 70113E
 Vercellone, S., Soldi, S., Chen, A.W., and Tavani, M., 2004, *MNRAS*, 353, 890
 Vercellone, S., D’Ammando, F., Vittorini, V., et al., 2008, *ApJ*, 676, L13
 Vercellone, S., D’Ammando, F., Vittorini, V., et al., 2010, *ApJ*, 712, 405
 Verrecchia, F., Pittori, C., Bulgarelli, A., et al., 2011, *Fermi Symposium proceedings*, eConf C110509, arXiv:1111.0025
 Vittorini, V., Tavani, M., Pucella, G., et al., 2010, *ApJ*, 732, L22

¹ ASI Science Data Center (ASDC), via del Politecnico snc, 00133 Roma, Italy.

² INAF-Osservatorio Astronomico di Roma, Via di Frascati 33, 00040 Monte Porzio Catone, Italy.

³ INAF/IASF Milano, via E. Bassini 15, 20133 Milano, Italy.

⁴ INAF/IASF Bologna, via Gobetti 101, 40129 Bologna, Italy.

⁵ INAF/IAPS, via del Fosso del Cavaliere 100, 00133 Roma, Italy.

⁶ Dip.di Fisica, Università “Tor Vergata”, via della Ricerca Scientifica 1, 00133 Roma, Italy.

⁷ INFN-Roma “Tor Vergata”, via della Ricerca Scientifica 1, 00133 Roma, Italy.

⁸ Consorzio Interuniversitario Fisica Spaziale (CIFS), villa Gualino - v.le Settimio Severo 63, 10133 Torino, Italy.

⁹ Agenzia Spaziale Italiana, viale Liegi 26, 00198 Roma, Italy.

¹⁰ INAF-Osservatorio Astronomico di Cagliari, loc. Poggio dei Pini, strada 54, 09012, Capoterra (CA), Italy.

¹¹ INAF-IASF Palermo, Via Ugo La Malfa 153, 90146 Palermo, Italy.

¹² Dip. Fisica, Università di Trieste, via A. Valerio 2, 34127 Trieste, Italy.

¹³ INFN Trieste, Padriciano 99, 34012 Trieste, Italy.

¹⁴ INFN Pavia, via A. Bassi 6, 27100 Pavia, Italy.

¹⁵ Dip. di Fisica, Università di Torino, via P. Giuria 15, 10126 Torino, Italy.

¹⁶ ENEA Bologna, via don Fiammelli 2, 40128 Bologna, Italy.

¹⁷ INFN Roma 1, p.le Aldo Moro 2, 00185 Roma, Italy.

¹⁸ Dip. Fisica, Università “La Sapienza”, p.le Aldo Moro 2, 00185 Roma, Italy.

¹⁹ ENEA Frascati, via Enrico Fermi 45, 00044 Frascati (RM), Italy.

²⁰ CNR, IMIP, Area Ricerca Montelibretti (RM), Italy.

²¹ Dip. Fisica, Università dell’Insubria, Via Valleggio 11, 22100 Como, Italy.

²² ASTRON, the Netherlands Institute for Radio Astronomy, Postbus 2, 7990 AA, Dwingeloo, The Netherlands

²³ Wits University, 1 Jan Smuts Avenue Braamfontein 2000, Johannesburg, South Africa.

Supplementary Table (Table 5)

Table 5. The variability results for the revised AGILE bright γ -ray sources list over the pointing-mode dataset. Column descriptions are provided at the end of the table.

AGILE name	R.A. (J2000.0) (hh mm ss)	Dec. (J2000.0) (dd mm ss)	L1,II,BII ($^{\circ}$ Error Rad.) ($^{\circ}$)	b TIME year.day	\sqrt{TS}	d Flux \pm Error	e IAGL Flux	$^fV, ^gV_{\text{obs}}, V_{\text{ys}2r}$ Mc L. indices	$^hF_{\text{sys}}$	i Num. det.	Class	Confirmed Counterp.	IAGL&Possible Association
	Start MJD	End MJD	OB Num.	c MeanOB Exp.	\sqrt{TS}	c Flux \pm Error /U.L.	Off-axis angle ($^{\circ}$)						
IAGLR J0007+7307	00 07 03.6	73 06 51.6	119.67, 10.52 (0.08)	2009.039	9.1	32.3 \pm 4.5	23.0	0.1, 0.05/0.05	6.41	13	Pulsar	PSRJ0007+7303	IAGLJ0006+7311 3EGJ0010+7309 2FGLJ0007.0+7303
	54308.5	54311.5	1150	21.8	4.55	83.7 \pm 25.0	21.8						
	54347.5	54355.5	2300	59.7	3.68	30.4 \pm 10.3	17.3						
	54439.4	54449.5	4910	74.4	3.89	35.2 \pm 11.3	38.3						
	54586.5	54596.5	5700	75.6	5.32	47.2 \pm 11.5	29.1						
	54596.5	54626.7	5800	201.1	4.81	31.3 \pm 7.8	43.5						
	54632.5	54647.5	5820	114.5	5.22	31.0 \pm 7.4	26.2						
	54678.5	54693.5	5920	110.6	3.62	27.1 \pm 8.9	37.8						
	54709.5	54719.5	6110	72.3	3.21	27.9 \pm 10.7	41.6						
	54820.5	54843.7	6600	153.4	5.24	28.0 \pm 6.6	29.2						
	54850.7	54890.5	6720	256.2	9.12	32.3 \pm 4.5	2.4						
	54997.5	55007.5	7500	73.0	4.47	37.0 \pm 10.4	32.2						
	55007.5	55027.5	7600	137.2	5.13	33.4 \pm 8.0	34.9						
	55027.5	55055.5	7700	201.4	8.38	32.9 \pm 5.0	7.6						
IAGLR J0135+4759	01 35 01.7	47 58 39.6	130.43, -14.26 (0.24)	2009.186	3.7	20.1 \pm 6.4	0.0	0.5, 0.44/0.13	5.99	10	—	S40133+47 BZQJ0019+7327 2FGLJ0136.9+4751	
	54308.5	54311.5	1150	21.8	2.20	<61.1	8.7						
	54439.4	54449.5	4910	74.4	3.44	43.2 \pm 14.9	40.2						
	54672.7	54678.5	5910	41.6	2.17	<41.8	9.5						
	54678.5	54693.5	5920	110.6	2.03	<27.0	12.7						
	54709.5	54719.5	6110	72.3	3.09	31.2 \pm 12.0	31.4						
	54800.5	54820.5	6500	119.7	2.61	<47.0	40.3						
	54820.5	54843.7	6600	153.4	2.82	<30.4	24.1						
	54850.7	54890.5	6720	256.2	2.14	<24.2	28.7						
	55007.5	55027.5	7600	137.2	3.75	20.1 \pm 6.4	22.0						
	55027.5	55055.5	7700	201.4	3.30	16.8 \pm 5.8	26.0						
IAGLR J0222+4305	02 22 12.2	43 04 37.8	140.05, -16.76 (0.21)	2008.249	4.0	32.8 \pm 10.2	0.0	0.5, 0.44/0.28	4.15	7	—	3C66A BZB10222+4302 TeVJ0222+430 TeVJ0223+430 2FGLJ0222.6+4302	
	54305.5	54308.5	1100	21.3	2.67	<81.9	12.7						
	54356.5	54358.5	2500	14.3	1.98	<118.4	30.3						
	54632.5	54647.5	5820	114.5	3.70	43.0 \pm 13.9	42.8						
	54678.5	54693.5	5920	110.6	3.31	19.3 \pm 6.8	3.9						
	54709.5	54719.5	6110	72.3	4.04	32.8 \pm 10.2	24.4						
	54850.7	54890.5	6720	256.2	3.40	19.6 \pm 6.6	35.9						
	55007.5	55027.5	7600	137.2	2.47	<34.7	29.8						
IAGLR J0240+6115	02 40 10.6	61 14 44.9	135.63, 1.08 (0.32)	2009.210	10.5	103.4 \pm 11.1	54.0	2.7, 1.54/1.1	18.10	12	HMXB	LS 1+61 $^{\circ}$ 303	IAGLJ0242+6111 TeVJ0240+612 3EGJ0241+6103 2FGLJ0240.5+6113
	54305.5	54308.5	1100	21.3	3.65	85.0 \pm 29.5	27.1						

Table 5. Continued. Column descriptions are provided at the end of the table.

AGILE name	R.A. (J2000.0) (hh mm ss)	Dec. (J2000.0) (dd mm ss)	L.I.II ($^{\circ}$ Error Rad.) ($^{\circ}$)	b TIME year.day	\sqrt{TS}	d Flux \pm Error	e IAGL Flux	$^fV, ^gV_{\text{obs}}, V_{\text{sys}}, V_{\text{sys}2\sigma}$ Mc L. indices	$^hF_{\text{sys}}$ det.	i Num. det.	Class	Confirmed Counterp.	IAGL&Possible Association
	Start MJID	End MJID	OB Num.	c MeanOB Exp.	\sqrt{TS}	c Flux \pm Error /U.L.	Off-axis angle ($^{\circ}$)						
	54678.5	54693.5	5920	110.6	11.01	222.5 \pm 26.5	43.6						
	54709.5	54719.5	6110	72.3	14.14	215.0 \pm 21.5	25.2						
	54921.5	54928.5	6910	50.2	12.54	231.9 \pm 26.0	23.7						
	55084.5	55087.5	8000	5.75	160.9 \pm 38.5	15.9							
	55087.5	55090.5	8100	22.4	8.58	234.8 \pm 38.8	25.2						
IAGL J0539-4358	05 38 32.3	-43 58 14.4	249.94, -31.13	(0.25)	2008.287	6.0	56.5 \pm 13.3	1.1 1.05/1.40	11.64	6	BL Lac	PKS0537-441	IAGLJ0538-4424 BZB0538-4405 3EGJ0540-4402 2FGLJ0538.8-4405
	Start MJID	End MJID	OB Num.	c MeanOB Exp.	\sqrt{TS}	c Flux \pm Error /U.L.	Off-axis angle ($^{\circ}$)						
	54311.5	54313.5	1200	14.9	2.30	<158.0	42.0						
	54358.5	54359.5	2600	6.1	3.61	142.9 \pm 54.9	21.0						
	54369.5	54370.5	3700	6.5	3.50	144.4 \pm 59.6	32.0						
	54497.5	54505.4	5200	51.7	2.06	<40.9	18.0						
	54749.5	54756.5	6210	50.2	6.05	56.5 \pm 13.3	11.9						
	54966.5	54976.7	7300	68.6	3.12	34.4 \pm 13.4	45.0						
IAGL J0617+2236	06 17 21.8	22 36 14.3	189.04, 3.07	2008.093	5.7	79.1 \pm 18.6	69.0	0.3, 0.28/0.13	7.68	13	SNR	IC443	IAGLJ0617+2236 3EGJ0617+2238 TeVJ0616+225 2FGLJ0617.2+223.4e
	Start MJID	End MJID	OB Num.	c MeanOB Exp.	\sqrt{TS}	c Flux \pm Error /U.L.	Off-axis angle ($^{\circ}$)						
	54334.5	54335.5	1700	6.1	2.44	<272.9	33.4						
	54344.5	54345.5	2000	6.6	1.98	<212.5	28.2						
	54355.5	54356.5	2400	6.6	4.65	182.3 \pm 57.5	13.0						
	54368.5	54369.5	3600	6.5	2.19	<213.7	25.5						
	54370.5	54374.5	3800	27.0	3.12	53.8 \pm 21.1	3.2						
	54374.5	54375.5	3900	6.9	3.05	120.2 \pm 52.3	5.5						
	54376.5	54377.5	4100	6.5	2.02	<180.9	17.2						
	54377.5	54385.5	4200	55.0	4.42	53.4 \pm 14.8	12.1						
	54555.5	54561.5	5000	36.2	5.73	79.1 \pm 18.6	10.6						
	54561.5	54563.5	5510	13.2	3.34	91.8 \pm 36.3	16.0						
	54564.5	54566.5	5530	13.4	3.18	68.7 \pm 29.1	17.3						
	54709.5	54719.5	6110	72.3	4.75	62.1 \pm 16.1	29.8						
	54921.5	54928.5	6910	50.2	4.51	54.9 \pm 15.2	15.2						
IAGL J0634+1748	06 34 15.9	17 48 27.8	195.14, 4.36	2007.281	28.6	381.4 \pm 23.7	320.0	1.2, 0.37/0.37	29.68	30	Pulsar	GEMINGA	IAGLJ0634+1748 3EGJ0633+1751 2FGLJ0633.9+1746
	Start MJID	End MJID	OB Num.	c MeanOB Exp.	\sqrt{TS}	c Flux \pm Error /U.L.	Off-axis angle ($^{\circ}$)						
	54334.5	54335.5	1700	6.1	7.64	408.7 \pm 92.0	37.7						
	54344.5	54345.5	2000	6.6	6.91	349.8 \pm 79.4	29.5						
	54345.5	54346.5	2100	6.7	11.22	536.1 \pm 87.1	27.1						
	54346.5	54347.5	2200	6.9	8.33	405.7 \pm 82.7	32.0						
	54355.5	54356.5	2400	6.6	10.16	491.7 \pm 84.0	17.6						
	54356.5	54358.5	2500	14.3	10.22	506.0 \pm 80.6	43.3						
	54360.5	54361.5	2800	4.5	7.10	308.0 \pm 76.7	13.1						
	54361.5	54362.5	2900	6.2	8.10	321.7 \pm 69.1	14.4						
	54362.5	54363.5	3000	6.7	8.25	330.8 \pm 69.5	21.7						
	54363.5	54364.5	3100	7.0	6.31	275.3 \pm 71.0	30.5						
	54364.5	54365.5	3200	7.2	8.78	479.1 \pm 96.6	39.9						

Table 5. Continued. Column descriptions are provided at the end of the table.

AGILE name	R.A. (J2000.0) (hh mm ss)	Dec. (J2000.0) (dd mm ss)	L.I.II (σ Error Rad.) ($^{\circ}$)	b TIME year.day	\sqrt{TS}	d Flux \pm Error	e IAGL Flux	$^fV, ^gV_{\text{ass3r}}, V_{\text{sys2r}}$ Me L. indices	$^hF_{\text{sys}}$ det.	Class	Confirmed Counterp.	IAGL&Possible Association
	Start MJD	End MJD	OB Num.	c MeanOB Exp.	\sqrt{TS}	c Flux \pm Error /U.L.	Off-axis angle ($^{\circ}$)					
	54366.5	54367.5	3400	6.6	8.41	292.2 \pm 61.1	7.7					
	54367.5	54368.5	3500	6.5	10.41	421.8 \pm 72.7	12.2					
	54368.5	54369.5	3600	6.5	8.67	388.1 \pm 75.3	21.3					
	54369.5	54370.5	3700	6.5	6.14	255.0 \pm 69.0	31.1					
	54370.5	54374.5	3800	27.0	19.45	355.8 \pm 32.4	4.3					
	54374.5	54375.5	3900	6.9	10.63	431.6 \pm 69.4	4.3					
	54375.5	54376.5	4000	6.8	10.28	456.0 \pm 78.5	19.2					
	54376.5	54377.5	4100	6.5	12.57	551.7 \pm 80.0	11.4					
	54377.5	54385.5	4200	55.0	28.64	381.4 \pm 23.7	9.1					
	54385.5	54386.5	4300	6.8	9.64	382.7 \pm 70.5	12.8					
	54395.5	54396.5	4500	5.4	9.55	510.4 \pm 94.2	22.6					
	54405.5	54406.5	4700	6.0	8.43	405.1 \pm 83.1	32.3					
	54555.5	54561.5	5500	36.2	22.18	333.5 \pm 27.2	7.7					
	54561.5	54563.5	5510	13.2	12.50	360.3 \pm 49.9	15.6					
	54564.5	54566.5	5530	13.4	14.39	372.7 \pm 47.3	13.8					
	54709.5	54719.5	6110	72.3	24.83	389.3 \pm 26.6	36.0					
	54921.5	54928.5	6910	50.2	25.86	363.9 \pm 25.0	16.3					
	55087.5	55087.5	8000	16.2	11.60	257.5 \pm 38.3	20.6					
	55087.5	55090.5	8100	22.4	14.20	309.8 \pm 36.8	25.3					
IAGLR J0713+3324	07 12 43.2	33 23 45.8	184.26, 18.66 (0.25)	2007.281	3.9	39.2 \pm 12.4	18.0	0.1, 0.05/0.11	3.21	7	—	IAGLJ0714+3341
	Start MJD	End MJD	OB Num.	c MeanOB Exp.	\sqrt{TS}	c Flux \pm Error /U.L.	Off-axis angle ($^{\circ}$)					
	54362.5	54363.5	3000	6.7	2.28	<172.8	17.4					
	54363.5	54364.5	3100	7.0	2.39	<164.3	20.3					
	54370.5	54374.5	3800	27.0	3.09	36.4 \pm 15.4	14.6					
	54374.5	54375.5	3900	6.9	2.15	<153.1	13.5					
	54377.5	54385.5	4200	55.0	3.89	39.2 \pm 12.4	11.9					
	54555.5	54561.5	5500	36.2	2.14	<46.2	12.0					
	54709.5	54719.5	6110	72.3	2.51	<46.1	31.7					
IAGLR J0723+7121	07 22 39.5	71 20 44.6	143.98, 28.08 (0.12)	2007.251	8.5	79.1 \pm 13.1	68.0	3.2, 2.53/2.42	22.67	9	BL Lac	IAGLJ0722+7126 BZBJ0721+7120 3EGJ0721+7120 TeVJ0721+7113 2FGLJ0721.9+7120
	Start MJD	End MJD	OB Num.	c MeanOB Exp.	\sqrt{TS}	c Flux \pm Error /U.L.	Off-axis angle ($^{\circ}$)					
	54347.5	54355.5	2300	59.7	8.33	79.1 \pm 13.1	15.2					
	54356.5	54358.5	2500	14.3	5.22	117.0 \pm 32.2	18.5					
	54362.5	54363.5	3000	6.7	2.13	<189.5	36.4					
	54363.5	54364.5	3100	7.0	2.65	<154.2	26.4					
	54364.5	54365.5	3200	7.2	4.25	140.9 \pm 46.3	16.7					
	54397.3	54402.5	4610	40.6	4.97	56.9 \pm 14.9	15.9					
	54586.5	54596.5	5700	75.6	4.07	40.6 \pm 12.4	35.7					
	54709.5	54719.5	6110	72.3	2.22	<42.6	33.4					
	55027.5	55055.5	7700	201.4	4.91	29.5 \pm 7.2	36.4					
IAGL J0835-4509	08 35 13.4	-45 09 09.0	263.52, -2.79	2008.195	61.1	911.5 \pm 25.2	780.0	0.8, 0.00/0.00	1.87	12	Pulsar	IAGLJ0835-4509 3EGJ0834-4511 2FGLJ0835.3-4510
	Start MJD	End MJD	OB Num.	c MeanOB Exp.	\sqrt{TS}	c Flux \pm Error /U.L.	Off-axis angle ($^{\circ}$)					

Table 5. Continued. Column descriptions are provided at the end of the table.

AGILE name	R.A. (J2000.0) (hh mm ss)	Dec. (J2000.0) (dd mm ss)	L.I.II ($^{\circ}$ Error Rad.) ($^{\circ}$)	b TIME year.day	\sqrt{TS}	d Flux \pm Error	e IAGL Flux	$^fV, ^gV_{\text{ass3r}}, V_{\text{sys2r}}$ Mc L. indices	$^hF_{\text{sys}}$	i Num. det.	Class	Confirmed Counterp.	IAGL&Possible Association
	Start MJD	End MJD	OB Num.	c MeanOB Exp.	\sqrt{TS}	c Flux \pm Error /U.L.	Off-axis angle ($^{\circ}$)						
	54294.5	54305.5	1000	75.9	45.32	874.4 \pm 33.7	26.6						
	54311.5	54313.5	1200	14.9	17.65	899.5 \pm 84.0	28.2						
	54314.5	54324.5	1400	59.1	32.00	856.7 \pm 44.3	36.7						
	54325.5	54334.5	1600	64.3	29.05	847.9 \pm 48.5	43.9						
	54473.5	54497.5	5100	131.2	55.92	816.1 \pm 25.0	26.3						
	54510.5	54526.5	5300	126.1	38.47	840.9 \pm 35.5	44.4						
	54647.5	54672.7	5900	167.2	61.09	911.5 \pm 25.2	33.4						
	54693.5	54709.5	6010	70.1	34.10	875.9 \pm 43.2	40.8						
	54749.5	54756.5	6210	50.2	36.77	841.1 \pm 39.4	19.2						
	54843.7	54850.7	6610	53.2	34.23	812.9 \pm 40.4	27.4						
	54966.5	54976.7	7300	68.6	49.66	940.9 \pm 33.3	0.83						
	54980.5	54986.5	7320	42.8	38.85	898.9 \pm 41.1	9.4						
IAGL J1018-5852	10 17 36.8	-58 51 36.9	284.16, -1.71 (0.25)	2008.195	3.6	44.1 \pm 12.9	0.0	-1.0, -1.0/0.06	2.47	7	—	—	PSR J1016-5857 2FGL J1019.0-5856 2FGL J1016.5-5858 G284.3-01.8
	Start MJD	End MJD	OB Num.	c MeanOB Exp.	\sqrt{TS}	c Flux \pm Error /U.L.	Off-axis angle ($^{\circ}$)						
	54294.5	54305.5	1000	75.9	1.99	<70.8	5.9						
	54314.5	54324.5	1400	59.1	1.96	<104.8	16.4						
	54335.5	54339.5	1800	30.2	2.48	<165.4	30.8						
	54510.5	54526.5	5300	126.1	2.24	<86.5	25.2						
	54647.5	54672.7	5900	167.2	3.62	44.1 \pm 12.9	17.2						
	54749.5	54756.5	6210	50.2	2.22	<148.1	33.4						
	54966.5	54976.7	7300	68.6	2.76	<95.6	23.7						
IAGL J1022-5751	10 21 33.3	-57 50 44.5	284.04, -0.58 (0.29)	2007.199	5.0	81.7 \pm 18.8	0.0	0.2, 0.15/0.42	5.31	6	—	—	TeV J1023-5777 3EG J1027-5817 2FGL J1022.7-5741 2FGL J1023.5-5749c
	Start MJD	End MJD	OB Num.	c MeanOB Exp.	\sqrt{TS}	c Flux \pm Error /U.L.	Off-axis angle ($^{\circ}$)						
	54294.5	54305.5	1000	75.9	4.99	81.7 \pm 18.8	6.0						
	54311.5	54313.5	1200	14.9	2.24	<153.9	13.0						
	54473.5	54497.5	5100	131.2	2.03	<88.0	7.0						
	54647.5	54672.7	5900	167.2	2.18	<59.1	16.3						
	54843.7	54850.7	6610	53.2	3.46	69.8 \pm 22.7	6.8						
	54966.5	54976.7	7300	68.6	2.19	<96.3	22.9						
IAGL J1022-5825	10 21 37.4	-58 25 21.0	284.36, -1.06 (-)	2009.233	3.8	91.1 \pm 22.8	59.0	0.1, -0.08/0.08	1.48	5	—	—	IAGL J1022-5822 3EG J1013-5915 TeV J1023-5777 2FGL J1019.0-5856 2FGL J1023.5-5749c 2FGL J1022.7-5741 2FGL J1016.5-5858 2FGL J1028.5-5819 PSR J1016-5819 G284.3-01.8 PSR J1016-5857
	Start MJD	End MJD	OB Num.	c MeanOB Exp.	\sqrt{TS}	c Flux \pm Error /U.L.	Off-axis angle ($^{\circ}$)						
	54314.5	54324.5	1400	59.1	3.40	84.3 \pm 21.6	16.3						
	54510.5	54526.5	5300	126.1	2.18	<99.9	25.3						

Table 5. Continued. Column descriptions are provided at the end of the table.

AGILE name	R.A. (J2000.0) (hh mm ss)	Dec. (J2000.0) (dd mm ss)	L.I.II ($^{\circ}$ Error Rad.) ($^{\circ}$)	b TIME year.day	\sqrt{TS}	d Flux \pm Error /U.L.	e IAGL Flux	$^fV, ^gV_{\text{axis}}, V_{\text{sys}}, V_{\text{sys}2\sigma}$ Mc L. indices	$^hF_{\text{sys}}$	i Num. det.	Class	Confirmed Counterp.	IAGL&Possible Association
	Start MJD	End MJD	OB Num.	c MeanOB Exp.	\sqrt{TS}	c Flux \pm Error /U.L.	Off-axis angle ($^{\circ}$)						
	54693.5	54709.5	6010	70.1	2.54	<123.9	22.9						
	54980.5	54986.5	7320	42.8	2.19	<157.9	20.2						
	55055.5	55074.5	7800	137.7	3.78	91.1 \pm 22.8	29.7						
IAGL J1044-5944	10 44 25.9	-59 44 01.4	287.55, -0.71	(0.25)	2007.199	4.8	68.5 \pm 16.5	27.0	1.1, 0.95/0.93	8.79	6	CWB	Eta Car 1AGLJ1044-5937 2FGLJ1045.0-5941
	Start MJD	End MJD	OB Num.	c MeanOB Exp.	\sqrt{TS}	c Flux \pm Error /U.L.	Off-axis angle ($^{\circ}$)						
	54294.5	54305.5	1000	75.9	4.80	68.5 \pm 16.5	2.5						
	54510.5	54526.5	5300	126.1	2.28	<51.9	22.6						
	54693.5	54709.5	6010	70.1	3.13	51.0 \pm 18.3	20.7						
	54749.5	54756.5	6210	50.2	4.31	112.5 \pm 30.4	36.8						
	54843.7	54850.7	6610	53.2	2.50	<85.8	3.3						
	55055.5	55074.5	7800	137.7	3.17	35.5 \pm 12.3	26.5						
IAGL J1048-5843	10 47 32.8	-58 42 43.6	287.43, 0.38	(0.29)	2007.219	3.9	77.7 \pm 22.9	0.0	-1.0, -1.0/0.63	4.26	4	—	PSR J1048-5832 3EG J1048-5840 2FGL J1048.2-5831
	Start MJD	End MJD	OB Num.	c MeanOB Exp.	\sqrt{TS}	c Flux \pm Error /U.L.	Off-axis angle ($^{\circ}$)						
	54314.5	54324.5	1400	59.1	3.86	77.7 \pm 22.9	13.8						
	54335.5	54339.5	1800	30.2	2.69	<138.3	27.9						
	54647.5	54672.7	5900	167.2	2.75	<51.1	13.8						
	54966.5	54976.7	7300	68.6	2.40	<90.3	25.4						
IAGL J1058-5239	10 58 31.1	-52 39 47.4	286.15, 6.49	2008.053	6.4	59.3 \pm 11.5	29.0	0.4, -0.26/0.11	7.37	12	Pulsar	PSR J1057-5226 1AGL J1058-5239 3EG J1058-5234 2FGL J1057.9-5226	
	Start MJD	End MJD	OB Num.	c MeanOB Exp.	\sqrt{TS}	c Flux \pm Error /U.L.	Off-axis angle ($^{\circ}$)						
	54294.5	54305.5	1000	75.9	3.63	30.6 \pm 10.1	8.5						
	54311.5	54313.5	1200	14.9	2.86	<134.5	18.9						
	54314.5	54324.5	1400	59.1	3.54	34.8 \pm 12.2	18.1						
	54473.5	54497.5	5100	131.2	4.94	33.9 \pm 8.2	11.6						
	54510.5	54526.5	5300	126.1	6.44	59.3 \pm 11.5	28.0						
	54647.5	54672.7	5900	167.2	5.14	28.7 \pm 6.6	9.5						
	54693.5	54709.5	6010	70.1	3.19	31.8 \pm 12.0	26.9						
	54749.5	54756.5	6210	50.2	2.77	<95.0	40.2						
	54843.7	54850.7	6610	53.2	4.53	52.2 \pm 14.5	8.1						
	54966.5	54976.7	7300	68.6	2.93	<57.6	22.0						
	54980.5	54986.5	7320	42.8	2.34	<59.6	20.5						
	55055.5	55074.5	7800	137.7	4.95	39.5 \pm 9.7	29.4						
IAGL J1105+3818	11 04 46.5	38 18 00.6	179.58, 65.06	(0.35)	2008.164	3.7	39.8 \pm 13.9	42.0	-1.0, -1.0/0.53	1.09	2	Mkn421	1AGL J1104+3754 BZBJ1104+3812 3EG J1104+3809 2FGL J1104.4+3812
	Start MJD	End MJD	OB Num.	c MeanOB Exp.	\sqrt{TS}	c Flux \pm Error /U.L.	Off-axis angle ($^{\circ}$)						
	54626.7	54632.5	5810	38.2	3.72	39.8 \pm 13.9	19.0						
	54986.5	54997.5	7410	76.8	2.37	<43.2	28.8						

Table 5. Continued. Column descriptions are provided at the end of the table.

AGILE name	R. A. (J2000.0) (hh mm ss)	Dec. (J2000.0) (dd mm ss)	LJ, BII (Error Rad.) ($^{\circ}$, $^{\circ}$)	b TIME year.day	\sqrt{TS}	d Flux \pm Error /U.L.	e IAGL Flux	fV , $^gV_{\text{ass3r}}$, V_{sys2r} Mc L. indices	$^hF_{\text{sys}}$	i Num. det.	Class	Confirmed Counterp.	IAGL&Possible Association
IAGLR J1107-6115	11 06 31.5	-61 15 24.5	290.66, -0.91 (-)	2008.053	3.3	36.8 \pm 12.4	30.0	-1.0, -1.0/0.05	0.24	3	—	—	IAGLJ1108-6103 PSRJ1105-6107 PSRJ1104-6103 3EGJ1102-6103 2FGLJ1105.6-6114 2FGLJ1104.7-6036 2FGLJ1112.5-6105 2FGLJ1059.3-6118c 2FGLJ1112.1-6040 G290.1-0.8 G291.0-0.1
IAGLR J1112-6104	11 12 22.0	-61 04 21.3	291.24, -0.47 (0.37)	2008.020	4.3	41.5 \pm 10.9	30.0	0.0, -0.04/0.00	0.21	6	—	—	IAGLJ1108-6103 PSRJ1112-6103 2FGLJ1112.5-6105 2FGLJ1112.1-6040 G291.0-0.1
IAGL J1228+0142	12 28 59.5	01 42 41.4	290.04, 64.02	2008.164	3.2	48.1 \pm 18.6	24.0	0.9, -0.88/0.88	2.28	2	FSRQ	3C273	IAGLJ1228+0142 BZQJ1229+0203 3EGJ1229+0210 2FGLJ1229.1+0202
IAGL J1238+0406	12 38 31.0	04 06 14.3	294.74, 66.77	2007.361	4.1	25.4 \pm 7.4	25.0	-1.0, -1.0/-1.0	-1.00	1	—	—	IAGLJ1238+0406 BZQJ1239+0443 GB6J1239+0443 3EGJ1236+0457 2FGLJ1239.5+0443
IAGL J1256-0549	12 56 33.2	-05 49 42.6	305.27, 57.02	2007.192	10.2	185.0 \pm 27.3	65.0	6.4, 4.41/4.41	20.32	3	FSRQ	3C279	IAGLJ1256-0549 BZQJ1256-0547 3EGJ1255-0549 TeVJ1256-057 2FGLJ1256.1-0547

Table 5. Continued. Column descriptions are provided at the end of the table.

AGILE name	R. A. (J2000.0) (hh mm ss)	Dec. (J2000.0) (dd mm ss)	L.II,BII ($^{\circ}$ Error Rad.) ($^{\circ}$)	b TIME year.day	\sqrt{TS}	d Flux \pm Error /U.L.	e IAGL Flux	$^fV, ^gV_{\text{ass3r}}, V_{\text{sys2r}}$ Mc L. indices	$^hF_{\text{sys}}$ det.	i Num. det.	Class	Confirmed Counterp.	IAGL&Possible Association
Start MJD	End MJD	OB Num.	OB Num.	c MeanOB Exp.	\sqrt{TS}	c Flux \pm Error /U.L.	Off-axis angle ($^{\circ}$)						
54719.5	54749.5	6200		201.8	3.19	48.5 \pm 16.0	29.5						
16 25 19.9	-25 30 43.5	352.03, 16.36 (0.39)		2009.266	5.4	52.6 \pm 11.8	0.0	0.3, 0.28/0.93	8.81	6			OS-237.8 BZUJ1625-2527 3EGJ1626-2519 2FGLJ1625.7-2526
Start MJD	End MJD	OB Num.	OB Num.	c MeanOB Exp.	\sqrt{TS}	c Flux \pm Error /U.L.	Off-axis angle ($^{\circ}$)						
54339.5	54344.5	1900		35.7	2.83	<88.5	17.2						
54541.5	54555.5	5450		78.1	3.07	33.9 \pm 12.7	25.1						
54890.5	54915.5	6800		174.4	1.97	<31.8	15.8						
55055.5	55074.5	7800		137.7	2.56	<62.9	42.3						
55090.5	55104.5	8200		94.6	5.39	52.6 \pm 11.8	23.5						
55104.5	55119.5	8300		97.6	4.45	53.0 \pm 14.3	37.0						
16 39 05.5	-47 02 28.2	337.75, -0.15		2009.071	4.8	71.1 \pm 16.0	76.0	0.0, 0.00/0.01	3.88	13			IAGLJ1639-4702 HESSI1640-465 3EGJ1639-4702 2FGLJ1638.0-4703c 2FGLJ1640.5-4633 G337.8-0.1 G337.2+0.1
Start MJD	End MJD	OB Num.	OB Num.	c MeanOB Exp.	\sqrt{TS}	c Flux \pm Error /U.L.	Off-axis angle ($^{\circ}$)						
54325.5	54334.5	1600		64.3	3.28	97.9 \pm 32.6	30.7						
54335.5	54339.5	1800		30.2	2.10	<169.2	23.3						
54339.5	54344.5	1900		35.7	2.21	<145.1	7.9						
54510.5	54526.5	5300		126.1	3.54	75.5 \pm 22.8	32.3						
54526.5	54541.5	5400		102.6	4.06	75.6 \pm 20.0	6.4						
54541.5	54555.5	5450		78.1	3.81	85.9 \pm 24.5	26.6						
54693.5	54709.5	6010		70.1	2.97	<164.4	37.1						
54890.5	54915.5	6800		174.4	4.78	71.1 \pm 16.0	20.7						
54915.5	54921.5	6810		42.6	2.54	<170.5	29.6						
55055.5	55074.5	7800		137.7	2.46	<81.2	23.9						
55074.5	55084.5	7900		72.1	2.82	<115.7	11.4						
55090.5	55104.5	8200		94.6	3.36	77.8 \pm 24.8	29.6						
55104.5	55119.5	8300		97.6	3.41	81.8 \pm 26.0	38.2						
17 09 24.7	-44 28 50.9	343.07, -2.64		2008.269	14.7	123.6 \pm 10.9	121.0	0.1, 0.04/0.04	9.02	17	Pulsar	PSRJ1709-4429	IAGLJ1709-4428 3EGJ1710-4439 2FGLJ1709.7-4429
Start MJD	End MJD	OB Num.	OB Num.	c MeanOB Exp.	\sqrt{TS}	c Flux \pm Error /U.L.	Off-axis angle ($^{\circ}$)						
54314.5	54324.5	1400		59.1	4.06	99.2 \pm 29.2	42.8						
54325.5	54334.5	1600		64.3	7.54	154.9 \pm 26.3	35.6						
54335.5	54339.5	1800		30.2	3.35	94.4 \pm 33.2	28.2						
54339.5	54344.5	1900		35.7	8.35	181.0 \pm 29.1	12.1						
54386.5	54395.5	4400		59.6	4.54	97.0 \pm 25.7	41.9						
54510.5	54526.5	5300		126.1	9.15	125.2 \pm 17.4	36.5						
54526.5	54541.5	5400		102.6	10.32	112.6 \pm 14.1	7.0						
54541.5	54555.5	5450		78.1	9.28	122.5 \pm 17.2	20.9						
54693.5	54709.5	6010		70.1	7.19	140.7 \pm 25.5	41.1						
54719.5	54749.5	6200		201.8	14.73	123.6 \pm 10.9	20.2						

Table 5. Continued. Column descriptions are provided at the end of the table.

AGILE name	R.A. (J2000.0) (hh mm ss)	Dec. (J2000.0) (dd mm ss)	LJ,II (° Error Rad.) (°, °)	^b TIME year.day	\sqrt{TS}	^d Flux ± Error /U.L.	^e IAGL Flux	^f V, ^g V _{ass3r} , V _{ass2r} Mc L. indices	^h F _{sys}	ⁱ Num. det.	Class	Confirmed Counterp.	IAGL&Possible Association
	Start MJD	End MJD	OB Num.	^c MeanOB Exp.	\sqrt{TS}	^c Flux ± Error /U.L.	Off-axis angle (°)						
	54339.5	54344.5	1900	35.7	2.52	<216.4	32.5						C8.3-0.0 PSRJ1803-2137
	54386.5	54395.5	4400	59.6	2.76	<140.0	24.3						
	54526.5	54541.5	5400	102.6	2.98	<123.7	31.7						
	54541.5	54555.5	5450	78.1	2.88	<104.4	7.3						
	54719.5	54749.5	6200	201.8	3.67	48.9±14.1	6.9						
	54756.5	54770.5	6310	80.8	2.08	<119.2	41.1						
IAGLR J1807-2103	18 07 29.4	-21 03 20.9	9.30, -0.32 (-)	2009.071	4.4	81.5±19.9	0.0	-1.0, -1.0/0.23	3.70	6			HESSJ1804-216 2FGLJ1808.5-2037c 2FGLJ1805.6-2136e PSRJ1808-2057 G9.7-0.0 G9.9-0.8 G8.9+0.4 PSRJ1809-2109
	Start MJD	End MJD	OB Num.	^c MeanOB Exp.	\sqrt{TS}	^c Flux ± Error /U.L.	Off-axis angle (°)						
	54719.5	54749.5	6200	201.8	2.43	<74.5	7.6						
	54890.5	54915.5	6800	174.4	4.40	81.5±19.9	11.1						
	54915.5	54921.5	6810	42.6	2.38	<127.2	11.2						
	54928.5	54936.5	7010	56.3	2.28	<158.0	21.1						
	55074.5	55084.5	7900	72.1	2.24	<136.6	23.5						
	55104.5	55119.5	8300	97.6	2.19	<78.7	14.2						
IAGLR J1809-2333	18 09 23.0	-23 33 02.9	7.33, -1.91 (0.25)	2009.248	5.4	105.9±23.0	53.0	2.0, 1.65/0.66	13.08	11			IAGLJ1809-2333 3EGJ1809-2328 2FGLJ1809.8-2332
	Start MJD	End MJD	OB Num.	^c MeanOB Exp.	\sqrt{TS}	^c Flux ± Error /U.L.	Off-axis angle (°)						
	54339.5	54344.5	1900	35.7	2.59	<162.0	32.0						
	54386.5	54395.5	4400	59.6	5.00	115.8±26.9	23.5						
	54526.5	54541.5	5400	102.6	2.46	<88.5	30.3						
	54719.5	54749.5	6200	201.8	4.66	48.1±11.3	5.0						
	54756.5	54770.5	6310	80.8	2.33	<102.0	41.8						
	54890.5	54915.5	6800	174.4	3.23	35.3±11.8	9.7						
	54915.5	54921.5	6810	42.6	2.59	<106.9	9.1						
	54928.5	54936.5	7010	56.3	2.26	<92.4	20.8						
	55074.5	55084.5	7900	72.1	5.37	105.9±23.0	22.2						
	55090.5	55104.5	8200	94.6	3.27	45.2±15.1	0.3						
	55104.5	55119.5	8300	97.6	2.42	<67.5	13.5						
IAGLR J1822-1456	18 22 30.1	-14 56 11.8	16.38, -0.53 (-)	2009.266	4.7	92.5±21.6	86.0	-1.0, -1.0/0.21	0.99	3			IAGLJ1824-1455 TeVJ1826-148 3EGJ1824-1514 2FGLJ1819.3-1523 2FGLJ1826.3-1450 G16.4-0.5 G16.0-0.5 PSRJ1825-1446 G16.7+0.1

Table 5. Continued. Column descriptions are provided at the end of the table.

AGILE name	R.A. (J2000.0) (hh mm ss)	Dec. (J2000.0) (dd mm ss)	L.I.II (Error Rad.) ($^{\circ}$)	b TIME year.day	\sqrt{TS}	d Flux \pm Error /U.L.	e IAGL Flux	$^fV, ^gV_{\text{assr}}, V_{\text{sys}2r}$ Mc L. indices	$^hF_{\text{sys}}$ det.	i Num. det.	Class	Confirmed Counterp.	IAGL&Possible Association
	Start MJID	End MJID	OB Num.	c MeanOB Exp.	\sqrt{TS}	c Flux \pm Error /U.L.	Off-axis angle ($^{\circ}$)						
	54526.5	54541.5	5400	102.6	2.19	<118.0	39.4						
	54928.5	54936.5	7010	56.3	2.31	<124.9	18.3						
	55090.5	55104.5	8200	94.6	4.72	92.5 \pm 21.6	9.2						
IAGL J1827-1227	18 26 57.7	-12 46 58.6	18 79, -0.48	2009.071	5.2	82.4 \pm 17.1	79.0	0.5, 0.42/0.04	4.80	11	—	—	IAGL J1827-1227 PSRJ1826-1334 3EGJ1826-1302 2FGLJ1826.1-1256 G18.6-0.2 G18.1-0.1 G18.9-1.1
	Start MJID	End MJID	OB Num.	c MeanOB Exp.	\sqrt{TS}	c Flux \pm Error /U.L.	Off-axis angle ($^{\circ}$)						
	54386.5	54395.5	4400	59.6	3.40	97.2 \pm 31.0	20.4						
	54526.5	54541.5	5400	102.6	2.24	<120.2	41.8						
	54541.5	54555.5	5450	78.1	2.69	<109.0	16.0						
	54566.5	54586.5	5600	135.0	3.05	71.7 \pm 25.1	37.7						
	54719.5	54749.5	6200	201.8	3.00	44.9 \pm 15.7	16.1						
	54756.5	54770.5	6310	80.8	2.29	<118.4	31.0						
	54890.5	54915.5	6800	174.4	5.23	82.4 \pm 17.1	20.5						
	54928.5	54936.5	7010	56.3	2.83	<136.6	18.0						
	54936.5	54951.5	7100	88.8	2.69	<129.2	35.6						
	55090.5	55104.5	8200	94.6	4.36	90.9 \pm 22.7	11.6						
	55104.5	55119.5	8300	97.6	2.92	<101.2	14.2						
IAGL J1833-2057	18 33 22.9	-20 56 40.8	12.24, -5.60 (0.18)	2009.280	4.7	45.9 \pm 11.5	0.0	0.4, 0.35/0.19	5.97	9	FSRQ	PKS1830-210	BZQJ1833-2103 3EGJ1832-2110 2FGLJ1833.6-2104
	Start MJID	End MJID	OB Num.	c MeanOB Exp.	\sqrt{TS}	c Flux \pm Error /U.L.	Off-axis angle ($^{\circ}$)						
	54339.5	54344.5	1900	35.7	3.46	93.5 \pm 33.2	37.8						
	54386.5	54395.5	4400	59.6	2.38	<66.2	17.7						
	54526.5	54541.5	5400	102.6	2.78	<70.4	34.7						
	54719.5	54749.5	6200	201.8	4.55	31.6 \pm 7.8	9.0						
	54756.5	54770.5	6310	80.8	3.41	54.6 \pm 18.3	36.4						
	54890.5	54915.5	6800	174.4	4.05	31.4 \pm 8.7	15.7						
	54915.5	54921.5	6810	42.6	3.71	51.9 \pm 17.0	8.5						
	54928.5	54936.5	7010	56.3	3.78	49.2 \pm 15.5	15.0						
	55104.5	55119.5	8300	97.6	4.67	45.9 \pm 11.5	8.4						
IAGL J1836+5923**	18 36 16.7	59 23 44.2	88.85, 24.99	2009.039	12.9	55.7 \pm 6.1	45.0	0.8, 0.39/0.39	16.73	17	—	—	IAGL J1836+5923 3EGJ1835+5918 2FGLJ1836.2+5926
	Start MJID	End MJID	OB Num.	c MeanOB Exp.	\sqrt{TS}	c Flux \pm Error /U.L.	Off-axis angle ($^{\circ}$)						
	54406.5	54435.5	4800	176.7	9.95	48.0 \pm 6.8	32.0						
	54435.5	54439.4	4900	28.9	4.26	39.2 \pm 13.3	16.4						
	54439.4	54449.5	4910	74.4	5.29	39.4 \pm 10.4	37.8						
	54449.5	54450.5	4920	7.0	3.88	123.9 \pm 50.5	40.7						
	54505.4	54508.5	5210	22.8	5.66	67.7 \pm 18.5	17.5						
	54566.5	54586.5	5600	135.0	6.49	36.5 \pm 7.7	40.3						
	54586.5	54596.5	5700	82.6	8.26	52.5 \pm 9.3	15.6						
	54596.5	54626.7	5800	201.1	12.14	55.4 \pm 6.6	34.8						

Table 5. Continued. Column descriptions are provided at the end of the table.

AGILE name	R. A. (J2000.0) (hh mm ss)	Dec. (J2000.0) (dd mm ss)	L.I./B.II (° Error Rad.) (°)	OB Num.	LI, B.II (° Error Rad.) (°)	^b TIME year.day	\sqrt{TS}	^d Flux ± Error /U.L.	^e IAGL Flux	^f V, ^g V _{axis} , V _{sys2r} Me L. indices	^h F _{sys}	ⁱ Num. det.	Class	Confirmed Counterp.	IAGL&Possible Association
Start MJD	End MJD	OB Num.	OB Num.	^c MeanOB Exp.	^c Flux ± Error /U.L.	^c MeanOB Exp.	^c Flux ± Error /U.L.	Off-axis angle (°)	Off-axis angle (°)						
54632.5	54647.5	5820	5820	114.5	6.24	114.5	31.6±7.1	31.0							
54770.5	54800.5	6400	6400	183.5	12.72	183.5	61.4±7.0	29.5							
54800.5	54820.5	6500	6500	119.7	8.08	119.7	57.8±10.0	41.1							
54820.5	54843.7	6600	6600	153.4	8.18	153.4	60.7±10.1	43.2							
54850.7	54890.5	6720	6720	256.2	12.89	256.2	55.7±6.1	30.2							
54951.5	54966.5	7200	7200	103.4	8.34	103.4	58.0±9.8	34.9							
54997.5	55007.5	7500	7500	73.0	5.95	73.0	47.2±11.3	37.7							
55027.5	55055.5	7700	7700	201.4	10.33	201.4	48.3±6.5	30.6							
55119.5	55135.5	8400	8400	16.4	3.28	16.4	51.4±22.7	31.1							
IAGLR J1839-0550	18 39 01.2	-05 50 21.1	26.32, 0.09 (0.29)	2009.266	4.7	2009.266	92.1±21.8	0.0	0.5, 0.41/0.31	5.43	7				GS 1839-06 PSR J1838-0549 3EG J1837-0606 2FGL J1839.3-0558c 2FGL J1839.0-0539
54541.499	54555.499	5450	5450	904.	2.51	904.	<101.9	23.3							
54719.499	54749.499	6200	6200	2336.	3.25	2336.	43.1±14.0	23.6							
54756.499	54770.499	6310	6310	935.	3.60	935.	73.5±22.2	24.0							
54770.499	54800.499	6400	6400	2124.	3.60	2124.	89.7±26.8	45.3							
54890.499	54915.499	6800	6800	2019.	3.61	2019.	58.0±17.2	28.0							
55090.499	55104.499	8200	8200	1095.	4.65	1095.	92.1±21.8	19.1							
55104.499	55119.499	8300	8300	1130.	4.36	1130.	82.8±20.8	18.7							
IAGLR J1848+6709	18 48 23.7	67 09 14.1	97.54, 25.14 (0.15)	2009.001	5.5	2009.001	45.8±10.1	20.0	1.8, 1.49/1.69	21.12	11				IAGL J1846+6714 BZQ J1849+6705 2FGL J1849.4+6706
54347.5	54355.5	2300	2300	59.7	5.09	59.7	70.0±17.5	38.5							
54402.5	54405.5	4620	4620	23.5	2.35	23.5	<100.8	40.2							
54406.5	54435.5	4800	4800	176.7	3.18	176.7	19.2±6.9	36.6							
54435.5	54439.4	4900	4900	28.9	2.47	28.9	<64.8	18.2							
54596.5	54626.7	5800	5800	201.1	3.37	201.1	18.6±6.4	37.9							
54632.5	54647.5	5820	5820	114.5	4.83	114.5	35.2±9.0	29.8							
54770.5	54800.5	6400	6400	183.5	2.24	183.5	<25.8	35.1							
54800.5	54820.5	6500	6500	119.7	4.50	119.7	39.4±10.6	42.2							
54820.5	54843.7	6600	6600	153.4	5.51	153.4	45.8±10.1	40.9							
54850.7	54890.5	6720	6720	256.2	5.19	256.2	21.4±4.9	23.3							
55027.5	55055.5	7700	7700	201.4	2.94	201.4	<23.9	24.8							
IAGL J1856+0122	18 55 57.7	01 22 24.4	34.67, -0.38	2009.266	5.9	2009.266	119.0±22.9	123.0	0.7, 0.53/0.48	12.46	12	SNR	W44		IAGL J1856+0122 G34.7-0.4 3EG J1856+0114 2FGL J1855.9+0121e PSR J1856+0113
54386.5	54395.5	4400	4400	59.6	2.67	59.6	<114.7	23.8							
54566.5	54586.5	5600	5600	135.0	4.34	135.0	63.5±16.0	21.9							
54719.5	54749.5	6200	6200	201.8	4.44	201.8	59.2±14.5	31.7							
54756.5	54770.5	6310	6310	80.8	5.34	80.8	98.2±20.8	16.2							
54770.5	54800.5	6400	6400	183.5	2.53	183.5	<76.7	36.9							
54890.5	54915.5	6800	6800	174.4	2.08	174.4	<68.9	36.3							

Table 5. Continued. Column descriptions are provided at the end of the table.

AGILE name	R. A. (J2000.0) (hh mm ss)	Dec. (J2000.0) (dd mm ss)	L.I.II (Error Rad.) ($^{\circ}$)	b TIME year.day	\sqrt{TS}	d Flux \pm Error /U.L.	e IAGL Flux	$^fV, ^gV_{\text{ass3r}}, V_{\text{sys2r}}$ Mc L. indices	$^hF_{\text{sys}}$	i Num. det.	Class	Confirmed Counterp.	IAGL&Possible Association
Start MJID	End MJID	OB Num.	OB Num.	c MeanOB Exp.	\sqrt{TS}	c Flux \pm Error /U.L.	Off-axis angle ($^{\circ}$)						
55119.5	55135.5	8400		16.4	2.56	<159.1	16.8						
IAGLR J2021+4030	20 21 14.1	40 29 54.5	78.24, \pm 2.16 (0.06)	2008.146	15.3	158.0 \pm 13.0	120.0	5.9, 3.01/2.70	41.64	20	Pulsar & SNR in complex region	PSR J2021+4026, Gamm Cyg SNR	IAGLJ2022+4032 TeVJ2021+404 G78.2+2.1 2FGLJ2021.5+4026
Start MJID	End MJID	OB Num.	OB Num.	c MeanOB Exp.	\sqrt{TS}	c Flux \pm Error /U.L.	Off-axis angle ($^{\circ}$)						
54406.5	54435.5	4800		176.7	14.04	152.5 \pm 13.6	7.1						
54435.5	54439.4	4900		28.9	5.94	172.4 \pm 36.3	13.1						
54439.4	54449.5	4910		74.4	11.67	210.0 \pm 23.4	18.4						
54449.5	54450.5	4920		7.0	2.57	<389.8	22.6						
54566.5	54586.5	5600		135.0	11.50	154.0 \pm 16.6	21.9						
54586.5	54596.5	5700		75.6	3.37	78.9 \pm 26.4	40.0						
54596.5	54626.7	5800		201.1	15.31	158.0 \pm 13.0	11.3						
54632.5	54647.5	5820		114.5	3.03	76.4 \pm 26.6	21.0						
54756.5	54770.5	6310		80.8	6.04	117.5 \pm 23.2	31.1						
54770.5	54800.5	6400		183.5	4.30	82.3 \pm 20.1	6.8						
54800.5	54820.5	6500		119.7	3.38	84.6 \pm 26.3	21.0						
54820.5	54843.7	6600		153.4	5.98	84.2 \pm 16.2	32.0						
54850.7	54890.5	6720		256.2	9.73	123.5 \pm 15.2	39.9						
54936.5	54951.5	7100		88.8	6.43	100.3 \pm 18.6	25.3						
54951.5	54966.5	7200		103.4	11.71	171.0 \pm 18.6	11.0						
54976.7	54980.5	7310		21.9	2.70	<201.3	37.4						
54997.5	55007.5	7500		73.0	7.44	146.2 \pm 24.0	23.1						
55007.5	55027.5	7600		137.2	2.09	<134.0	39.0						
55027.5	55055.5	7700		201.4	10.29	145.1 \pm 17.1	35.5						
55119.5	55135.5	8400		16.4	2.63	<187.5	18.6						
IAGLR J2027-0747	20 26 46.2	-07 47 29.5	36.84, \pm 24.72 (0.21)	2007.320	5.2	56.6 \pm 14.3	39.0	1.0, 1.41/3.42	26.69	8		—	IAGLJ2026-0732
Start MJID	End MJID	OB Num.	OB Num.	c MeanOB Exp.	\sqrt{TS}	c Flux \pm Error /U.L.	Off-axis angle ($^{\circ}$)						
54386.5	54395.5	4400		59.6	5.20	71.0 \pm 16.8	14.4						
54396.5	54397.3	4600		4.7	3.00	168.6 \pm 75.8	9.9						
54406.5	54435.5	4800		176.7	5.24	56.6 \pm 14.3	41.7						
54566.5	54586.5	5600		135.0	3.27	28.8 \pm 10.2	30.9						
54596.5	54626.7	5800		201.1	2.37	<50.1	44.5						
54719.5	54749.5	6200		201.8	2.72	<40.9	37.9						
54756.5	54770.5	6310		80.8	2.55	<40.9	20.0						
54770.5	54800.5	6400		183.5	2.30	<40.5	42.1						
IAGLR J2030-0617	20 30 21.5	-06 17 23.5	38.76, \pm 24.84 (0.17)	2007.320	4.0	37.9 \pm 11.2	0.0	0.2, 0.17/0.17	0.17	2		—	BZQJ2030-0617 2FGLJ2030.3-0622
Start MJID	End MJID	OB Num.	OB Num.	c MeanOB Exp.	\sqrt{TS}	c Flux \pm Error /U.L.	Off-axis angle ($^{\circ}$)						
54386.5	54395.5	4400		59.6	3.58	46.2 \pm 15.4	16.1						
54406.5	54435.5	4800		176.7	3.96	37.9 \pm 11.2	40.2						
IAGLR J2031+4130	20 30 54.1	41 29 46.5	80.11, \pm 1.25 (0.18)	2009.186	3.2	63.0 \pm 19.5	0.0	-1.0, -1.0/0.30	4.35	6	Pulsar	PSRJ2032+4127	TeVJ2032+4130 2FGLJ2032.2+4126
Start MJID	End MJID	OB Num.	OB Num.	c MeanOB Exp.	\sqrt{TS}	c Flux \pm Error /U.L.	Off-axis angle ($^{\circ}$)						
54406.5	54435.5	4800		176.7	2.14	<39.3	7.6						
54632.5	54647.5	5820		114.5	2.02	<72.4	19.0						

Table 5. Continued. Column descriptions are provided at the end of the table.

AGILE name	R. A. (J2000.0) (hh mm ss)	Dec. (J2000.0) (dd mm ss)	LJ, BII (^e Error Rad.) (^c °)	^b TIME year.day	\sqrt{TS}	^d Flux \pm Error	^e IAGL Flux	^f V, ^g V _{var} , V _{sys2σ} Mc L. indices	^h F _{sys}	ⁱ Num. det.	Class	Confirmed Counterp.	IAGL&Possible Association
	Start MJID	End MJID	OB Num.	^c MeanOB Exp.	\sqrt{TS}	^e Flux \pm Error /U.L.	Off-axis angle (°)						
	54632.5	54647.5	5820	114.5	16.41	216.6 \pm 18.9	35.3						
	54672.7	54678.5	5910	41.6	13.61	376.0 \pm 41.6	41.9						
	54770.5	54800.5	6400	183.5	10.63	93.5 \pm 11.4	41.0						
	54800.5	54820.5	6500	119.7	9.05	69.7 \pm 10.3	22.1						
	54820.5	54843.7	6600	153.4	9.82	79.1 \pm 10.6	28.8						
	54951.5	54966.5	7200	103.4	5.57	59.4 \pm 13.5	37.0						
	54976.7	54980.5	7310	21.9	4.42	80.2 \pm 24.0	12.7						
	54997.5	55007.5	7500	73.0	4.92	52.3 \pm 13.5	27.8						
	55007.5	55027.5	7600	137.2	2.53	<31.3	24.9						

^a Positional error circle radius at 95% c.l., statistical error only. The AGILE team recommends adding a systematic error of ± 0.1 degrees linearly.
^b Start time in year.DoY.

^c Mean value of the exposure map relative to the OB map used for each source analysis in $\text{cm}^2 \text{ Ms}$.

^d E>100 MeV flux and its 1σ statistical error in $10^{-8} \text{ ph cm}^{-2} \text{ s}^{-1}$ units. The AGILE team recommends adding a systematic error of 10% to the statistical error.

^e E>100 MeV flux reported in IAGL in $10^{-8} \text{ ph cm}^{-2} \text{ s}^{-1}$ units.

^f McLaughlin V variability index (McLaughlin et al. 1996).

^g McLaughlin V variability indices calculated including a 10% systematic error and for the last value (after “^h”) also including detections at $2 \leq \sqrt{TS} < 3$.

^h A modified χ^2 including a 10% systematic error.

ⁱ Number of detections with $\sqrt{TS} \geq 2$.

* Pulsar + nebula.

** γ -ray source positionally consistent with the pulsar 2FGLJ1836.2+5926.